Mutations in *Vps15* perturb neuronal migration in mice and are associated with neurodevelopmental disease in humans

Thomas Gstrein[1], Andrew Edwards[2], Anna Přistoupilová [3,4,5], Ines Leca[1], Martin Breuss[1], Sandra Pilat-Carotta[1], Andi H. Hansen[1], Ratna Tripathy[1], Anna K. Traunbauer[1], Tobias Hochstoeger[1], Gavril Rosoklija[1], Marco Repic[6], Lukas Landler[1], Viktor Stránecký[3], Gerhard Dürnberger[1], Thomas M. Keane[7], Johannes Zuber[1], David J. Adams[7], Jonathan Flint[2], Tomas Honzik[8], Marta Gut[4,5], Sergi Beltran[4,5], Karl Mechtler[1], Elliott Sherr[9], Stanislav Kmoch[3], Ivo Gut[4,5] and David A. Keays [1]*

The formation of the vertebrate brain requires the generation, migration, differentiation and survival of neurons. Genetic mutations that perturb these critical cellular events can result in malformations of the telencephalon, providing a molecular window into brain development. Here we report the identification of an *N*-ethyl-*N*-nitrosourea-induced mouse mutant characterized by a fractured hippocampal pyramidal cell layer, attributable to defects in neuronal migration. We show that this is caused by a hypomorphic mutation in *Vps15* that perturbs endosomal–lysosomal trafficking and autophagy, resulting in an upregulation of Nischarin, which inhibits Pak1 signaling. The complete ablation of *Vps15* results in the accumulation of autophagic substrates, the induction of apoptosis and severe cortical atrophy. Finally, we report that mutations in *VPS15* are associated with cortical atrophy and epilepsy in humans. These data highlight the importance of the Vps15–Vps34 complex and the Nischarin–Pak1 signaling hub in the development of the telencephalon.

The formation of the vertebrate brain is a complex process that requires the generation and migration of neurons, followed by their differentiation and survival[1]. In the case of the cortex and hippocampus, neurogenesis occurs in the proliferative ventricular zones where radial glia and intermediate progenitors undergo extensive neurogenic divisions[2]. The resultant postmitotic neurons then begin a cellular journey, undertaking a series of genetically programmed morphological transitions before propelling themselves along the radial glia scaffold forming a laminar structure[3]. This migration requires the generation of polarity, extension of a leading process, translocation of the nucleus and retraction of the trailing process. Having reached their final destination, neurons mature through a process of differentiation that involves axon extension and the formation of dendritic processes.

Insight into the molecular mechanisms that mediate these critical cellular processes have been informed by the study of spontaneous and *N*-ethyl-*N*-nitrosourea (ENU)-induced mouse mutants[4]. For instance, the reeler mouse revealed the importance of the extracellular signaling protein Reelin[5], the scrambler mutant implicated the tyrosine phosphatase Dab1[6] and the *Tuba1a* mouse mutant has underlined the role of the microtubule cytoskeleton[7]. The study of engineered mouse mutants has also been pivotal, highlighting the role of nonreceptor protein kinases such as JNK and Cdk5[8]. Cdk5 sits at the intersection of a signaling pathway, phosphorylating molecules such as Dab1, Dcx, Map1b and Pak1[9]. Pak1, which is an

effector of Rac1 and Cdc42, has been implicated in the regulation of actin and microtubule dynamics. While these functional studies have advanced our understanding of the molecular mechanisms that mediate neuronal migration, it is nonetheless apparent that the picture is far from complete. In this study we established a genetic screen in mice to identify new genes required for telencephalic development, with a focus on neuronal migration. We report that mutations in *Vps15* impair the migration and survival of neurons in mice depending on the protein dosage and that mutations in the human homolog are associated with neurodevelopmental disease.

Results

ENU screen, genetic mapping and rescue. We performed a recessive ENU screen, undertaking a quantitative and qualitative analysis of structural brain phenotypes in the adult mouse brain (Fig. 1a). This screen employed Nissl staining and assessed such attributes as ventricular volume, cortical thickness, the thickness of hippocampal layers, corpus callosal volume and the presence of ectopic cells (Supplementary Fig. 1a). We screened a total of 38 pedigrees, each with at least 12 animals per line. Based on the observed rate of ENU-induced mutations, this represents approximately 2.7% coverage of the coding genes in the mouse genome[10]. We identified six pedigrees with a variety of neuroanatomical abnormalities, one of which presented with striking pyramidal cell ectopia in the hippocampus, reminiscent of *Tuba1a*, *Dcx* and *Lis1* mutant mice (Fig. 1d,e,g,h)[7,11,12].

[1]Institute of Molecular Pathology (IMP), Vienna Biocentre (VBC), Vienna, Austria. [2]Wellcome Trust Center for Human Genetics (WTCHG), Oxford, UK. [3]Institute of Inherited Metabolic Disorders, Charles University, Prague, Czech Republic. [4]CNAG-CRG, Centre for Genomic Regulation (CRG), Barcelona Institute of Science and Technology (BIST), Barcelona, Spain. [5]Universitat Pompeu Fabra (UPF), Barcelona, Spain. [6]Institute for Molecular Biotechnology (IMBA), Vienna, Austria. [7]Wellcome Trust Sanger Institute, Hinxton, Cambridgeshire, UK. [8]Department of Pediatrics and Adolescent Medicine, First Faculty of Medicine, Charles University, Prague, Czech Republic. [9]Institute of Human Genetics, University of California, San Francisco, San Francisco, CA, USA. *e-mail: keays@imp.ac.at
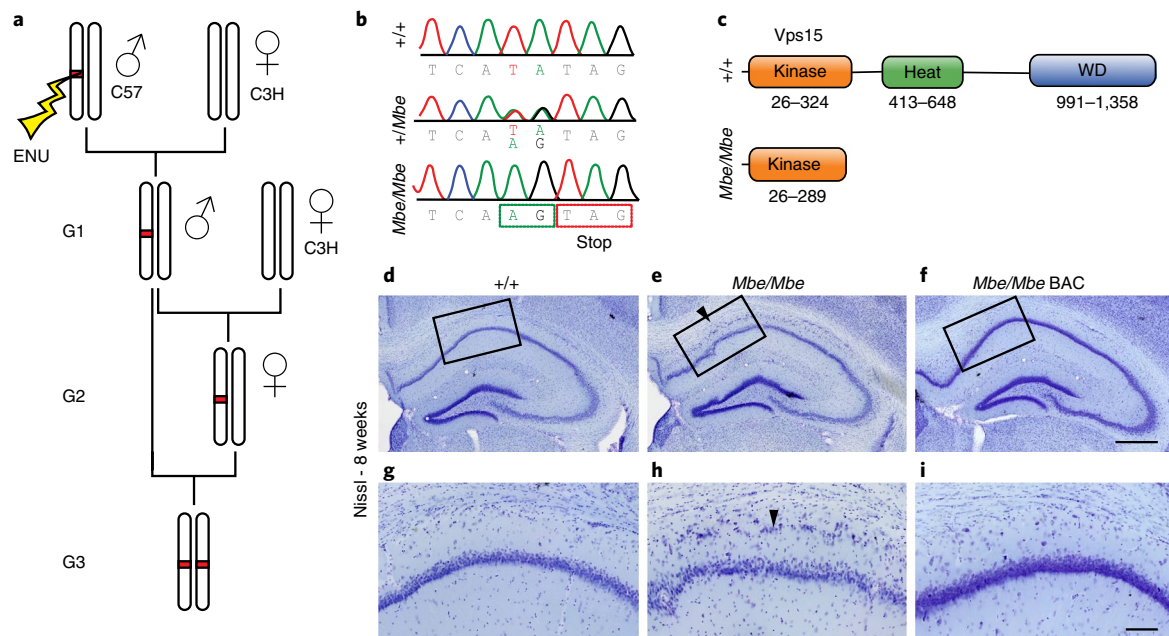
Fig. 1 | Vps15 is mutated in the Marble mouse. a, The Marble mouse was identified in a recessive ENU mutagenesis screen. ENU was injected into male C57/BL6 mice that were then crossed to C3H/HeH females. Male offspring (G1) were backcrossed to C3H/HeH females, and their daughters (G2) crossed to their G1 fathers. The resultant G3 offspring were subject to histological analysis (see Supplementary Fig. 1). **b**, The Marble mouse has a T-to-A substitution upstream of exon 4 of *Vps15* (GRCm38p4, chr9: 105,650,312). This mutation, coupled with a single-nucleotide polymorphism on the C57/BL6 background, results in a premature splice acceptor site, introducing a premature stop codon in *Mbe/Mbe* mutants. **c**, Structure of the Vps15 protein, which is 1,358 amino acids in length and has a putative kinase domain (26–342), four heat domains (413–648), and seven WD domains (991–1,358). **d–f**, Representative hippocampal Nissl stains of adult wild-type animals (**d**, control), Marble mutants (**e**, *Mbe/Mbe*), and mutants with additional copies of Vps15 delivered by genetic methods (**f**, *Mbe/Mbe* BAC). Scale bar, 500 μm. **g–i**, Magnified boxed regions of the images shown in **d–f**, respectively. The fractured pyramidal cell layer in the hippocampus that extends from CA1 to CA3 (arrowhead) in mutant animals is completely rescued by Vps15 overexpression. This experiment was performed three times with similar results. Scale bar, 100 μm. Experiments shown in **d–i** were repeated in 3 animals per genotype.

To identify the causative mutation in this recessive line, nicknamed Marble, we adopted a traditional positional cloning strategy employing microsatellite markers. This approach narrowed the genomic interval to a 28.6-Mb region on distal chromosome 9 that contains 439 genes (Supplementary Fig. 1b). Whole-exome sequencing failed to identify any coding variants within this region, but revealed the presence of a T-to-A substitution in the intron upstream of exon 4 of *Vps15* (GRCm38p4, chr9: 105,650,312; Fig. 1b). This mutation was not found in either of the strains used for mapping (C3H/HeH and C57/BL6J mice), nor is it reported to be a naturally occurring polymorphism in wild-type or inbred mice. The T-to-A mutation creates a novel splice acceptor site, which is predicted to introduce a premature stop codon resulting in a truncated protein of 289 amino acids (Fig. 1c). We extracted mRNA from the developing brain (at embryonic day (E) 14.5) of homozygous mutants (*Mbe/Mbe*) and confirmed the introduction of this stop codon into the transcript (Supplementary Fig. 1c). To formally test whether the mutation in *Vps15* is responsible for the fractured pyramidal cell layer in the Marble line, we performed a rescue experiment by creating a bacterial artificial chromosome (BAC) transgenic mouse that has additional copies of *Vps15*. We selected a BAC (RP24-281C16) that contains the complete sequence of *Vps15* and the partial sequence of the neighboring gene *Col6a6*. Following pronuclear injections and confirmation of germline transmission, we analyzed our BAC transgenic animals, confirming that the presence of additional copies of *Vps15* does not result in a neurological phenotype (Supplementary Fig. 1d–m). We then crossed our BAC transgenic mice into the Marble line. We found that homozygous *Mbe/Mbe* mutants with the BAC transgene were indistinguishable from wild-type controls

(Fig. 1d–i). Collectively, these data show that *Vps15* is necessary for neuronal migration in the murine hippocampus.

The *Mbe/Mbe* mutation impairs the function of the Vps15–Vps34 complex. Vps15 is known to form a complex with Vps34 and Beclin1, catalyzing the formation of the phospholipid PI(3)P, which is important for the maturation of endosomes as well as the formation of autophagosomes[13,14]. Its essential role in vesicular processes is reflected by its ubiquitous expression pattern, which we confirmed by quantitative PCR (qPCR) (Supplementary Fig. 2a–c). To assess whether the Marble mutation perturbs the Vps15–Vps34–Beclin1 complex we extracted protein lysates from the developing mouse forebrain (E14.5) and mouse embryonic fibroblasts (MEFs) and performed western blot analysis. This revealed a large reduction in the total protein levels of full-length Vps15 and its binding partners Vps34 and Beclin1 in *Mbe/Mbe* mutants in the developing forebrain and in MEFs (Fig. 2a,b and Supplementary Fig. 2d,e). We were not able to detect a truncated form of the Vps15 protein in *Mbe/Mbe* MEF lysates using an N-terminal antibody (Supplementary Fig. 2g,h). An assessment of *Vps15* transcript levels in the developing forebrain (E14.5) of *Mbe/Mbe* mutants revealed a reduction in *Vps15* mRNA consistent with nonsense mediated degradation; however, this reduction was not statistically significant ($P = 0.2$; Supplementary Fig. 2f and Supplementary Tables 1 and 2). Transcript levels of *Vps34* and *Beclin1* were similar in *Mbe/Mbe* mutants and wild-type controls, indicating that the downregulation of these proteins was a consequence of post-transcriptional dysfunction. To assess the effect of the *Mbe/Mbe* mutation on endosomal trafficking, we performed an epidermal growth factor
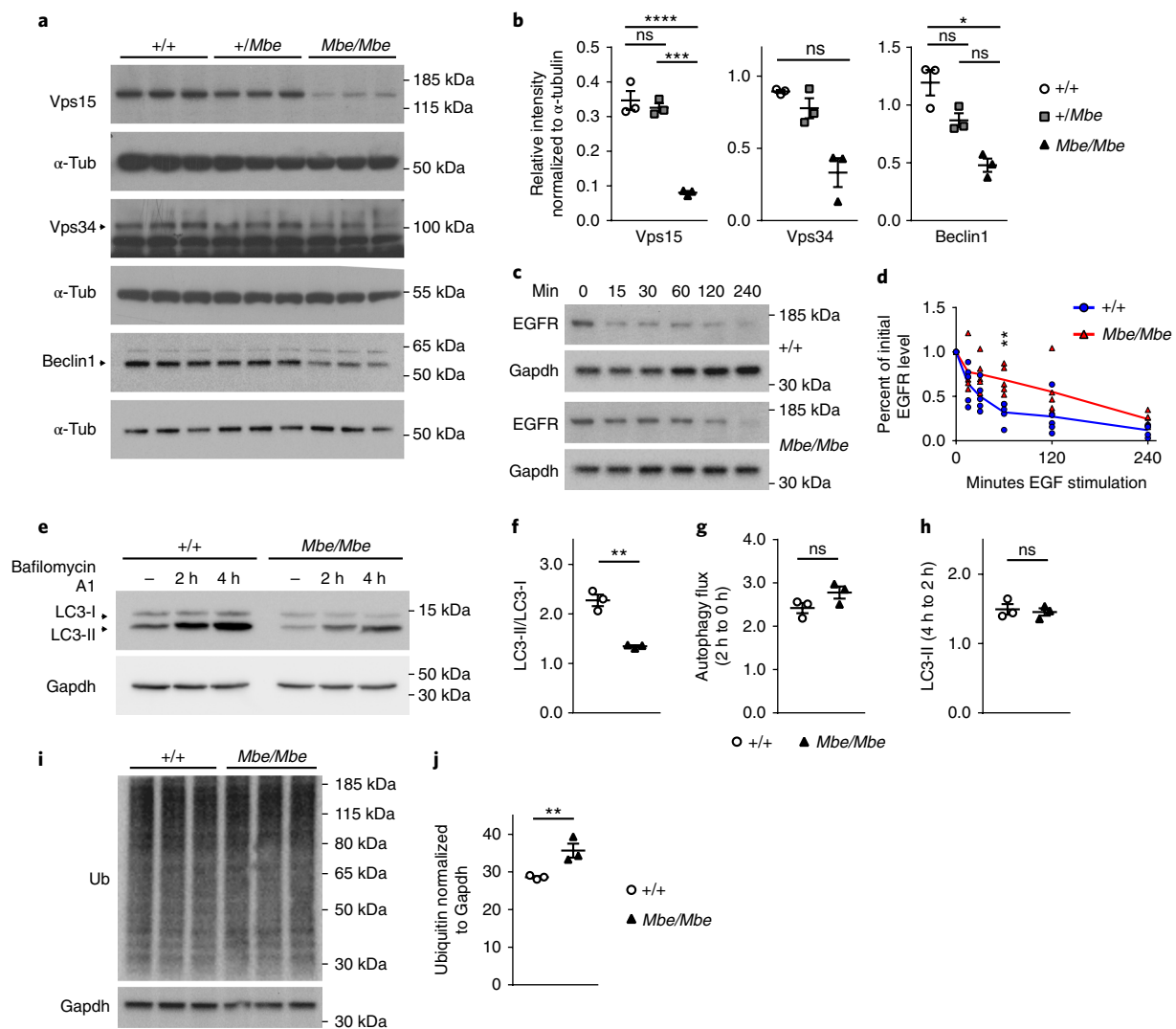
Fig. 2 | The *Mbe/Mbe* mutation compromises the function of the Vps15/Vps34 complex. a, Western blot analysis of Vps15 and its interacting partners Vps34 and Beclin1 from E14.5 brain lysates reveals a dramatic reduction in protein levels in *Mbe/Mbe* mutants ($n = 3$ animals per genotype). **b**, Quantification of western blot results shows that the reduction of Vps15 and Beclin1 protein levels is significant ($n = 3$ animals per genotype; Vps15: one-way ANOVA with Tukey's multiple-comparison test; control vs. *Mbe/Mbe*, $P < 0.0001$; +/*Mbe* vs. *Mbe/Mbe*, $P = 0.0002$; Beclin1: Kruskal–Wallis test with Dunn's multiple-comparison test; control vs. *Mbe/Mbe*, $P = 0.034$). Protein levels of Vps34 are greatly reduced, but this difference is not statistically significant ($n = 3$ animals per genotype; Kruskal–Wallis test with Dunn's multiple-comparison test; control vs. *Mbe/Mbe*, $P = 0.076$). This experiment was performed twice with similar results. α-Tub, α-tubulin. **c,d**, EGF was employed to stimulate EGFR endocytosis and degradation in MEFs isolated from *Mbe/Mbe* mutants and littermate controls. Levels of EGFR were monitored over 4 h and normalized to Gapdh. Over time we observed a degradation of EGFR in wild-type control cells that was almost undetectable at 240 min (**c**). This contrasts with *Mbe/Mbe* mutants, in which higher levels of EGFR were present at all timepoints (**d**), indicative of a defect in endosome to lysosome trafficking ($n = 5$ animals per genotype; two-way repeated-measures ANOVA with Bonferroni multiple-comparison test, $F_{1,8} = 7.694$; overall effect of genotype: $P = 0.024$; at 60 min: $P = 0.008$). **e–h**, Western blot analysis of LC3-I and LC3-II on protein lysates isolated from MEFs normalized to Gapdh. Quantification (**f–h**) shows a significant reduction in the ratio of LC3-II/LC3-I before incubation with bafilomycin A1 ($n = 3$ animals per genotype; unpaired two-tailed t test, Bonferroni corrected; $t_4 = 7.879$, $P = 0.004$) but no significant difference in autophagy flux ($n = 3$ animals per genotype; autophagy flux (0–2 h): unpaired two-tailed t test, Bonferroni corrected; $t_4 = 1.958$, $P = 0.365$; LC3-II (2–4 h): unpaired two-tailed t test; $t_4 = 0.4196$, $P > 0.5$). These data indicate there is a smaller pool of autophagosomes in *Mbe/Mbe* mutant cells. **i**, Western blot analysis of ubiquitinated (ub) proteins on lysates isolated from MEFs. **j**, Quantification shows an upregulation of ubiquitinated proteins in *Mbe/Mbe* mutants ($n = 3$ animals per genotype; one-tailed unpaired t test; $t_4 = 3.762$, $P = 0.01$). *$P < 0.05$; **$P < 0.01$; ***$P < 0.001$; ****$P < 0.0001$; ns, not significant. All immunoblots shown are cropped; for full-length blots see Supplementary Fig. 11. Error bars show mean ± s.e.m.

receptor (EGFR) assay in MEFs[15]. Treatment of MEFs with epidermal growth factor (EGF) results in a near complete degradation of the EGF–EGFR complex as internalized endosomes fuse with lysosomes. We pulsed MEFs with EGF and monitored the levels of EGFR over 4 h with normalization to Gapdh. We observed a rapid decrease in the levels of EGFR in wild-type cells that was absent in *Mbe/Mbe* mutants, most notably at 60 min (Fig. 2c,d). Consistent

with this result, we observed an increased half-life of the PDGF receptor in *Mbe/Mbe* mutant MEFs following stimulation with the ligand PDGF-BB[16] (Supplementary Fig. 2i,j). An assessment of lysosomal function using LysoTracker revealed no difference between genotypes (Supplementary Fig. 2k,l). Together, these data indicate that the mutation in *Vps15* compromises endosome to lysosome trafficking but not lysosomal function.

Next, we assessed the effect of the *Mbe/Mbe* mutation on autophagy, by undertaking LC3 western blot analysis of protein lysates from MEFs (Fig. 2e–h). Autophagosomes are associated with the lipidation of the cytosolic form of LC3 (LC3-I), forming LC3-II. Following the fusion of autophagosomes with lysosomes, LC3-II is degraded by lysosomal proteases[17]. Consistent with a reduction in the number of autophagosomes, we observed a decreased ratio of LC3-II to LC3-I in *Mbe/Mbe* mutants (Fig. 2e,f). We assessed autophagy flux by incubating *Mbe/Mbe* MEFs with bafilomycin A1, which inhibits the fusion of autophagosomes with lysosomes. Analysis of LC3-II levels at 2 and 4 h relative to Gapdh levels revealed no differences in the flux of autophagosomes in *Mbe/Mbe* MEFs. These data indicate that there is a reduction in the initial pool of autophagosomes in *Mbe/Mbe* animals. Previous studies have shown that defects in autophagy can result in the accumulation of ubiquitinated substrates[18]. To ascertain whether this occurs in *Mbe/Mbe* mutants, we performed western blot analysis of MEF protein lysates with a ubiquitin antibody. This revealed a mild, but significant, upregulation of ubiquitinated proteins in *Mbe/Mbe* MEFs ($n = 3$, $P = 0.01$; Fig. 2i,j). These data show that the *Mbe/Mbe* mutation compromises the function of the Vps15–Vps34 complex, impairing endosomal-to-lysosomal trafficking, accompanied by a reduction in the pool of autophagosomes.

Hippocampal proteomics reveals that Nischarin–Pak1 signaling is perturbed in *Mbe/Mbe* animals. To gain further insight into the molecular mechanisms, we assessed the impact of the *Vps15* mutation on the global proteome of the developing hippocampus in *Mbe/Mbe* mutants. We chose to analyze mice at postnatal day (P) 0, as pyramidal cell neurogenesis peaks at E14 to E16 and the subsequent migration takes 5–7 d. Extracted protein samples from P0 hippocampi from wild-type and mutant animals ($n = 3$ replicates per genotype) were digested with trypsin, labeled with tandem mass tags and subjected to mass spectrometry (Fig. 3a). We generated a total of 1.1 million spectra, enabling the identification of 51,506 unique peptides. We observed at least 49,000 peptides in each sample, which were then mapped to 7,566 Swiss-Prot accessions. We employed this dataset as a discovery tool, applying a modified *t* test that incorporates a Bayesian approach[19]. We set a threshold of $P < 0.01$, resulting in the identification of 91 proteins that were more abundant and 96 that were less abundant in the *Mbe/Mbe* hippocampus (Supplementary Table 3). Consistent with results from our western blot experiments, we observed that Beclin1, Vps15 and Vps34 were all less abundant (Fig. 3b). We employed the Ingenuity software platform (Qiagen) to identify those proteins associated with cell movement ($n = 18$ proteins). We then manually annotated each of these proteins, drawing on the published literature, and identified six dysregulated proteins known to be involved in neuronal migration (RhoA, Jam3, Nischarin, Slit2, Fgfr3 and Ephb3), one of which (Nischarin) also harbored a phosphoinositol binding domain (Fig. 3c). We confirmed that Nischarin is more abundant in the *Mbe/Mbe* hippocampus, cortex and E14.5 forebrain by western blot analysis (Fig. 3d,e). In contrast, the levels of *Nischarin* mRNA were similar when comparing *Mbe/Mbe* mutants and controls, indicative of post-translational dysregulation (Fig. 3f). Nischarin is broadly expressed at low levels in adult organs, but is enriched in the developing mouse brain (Supplementary Fig. 3a,b). It is a cytoplasmic protein with a PX domain that binds PI(3)P, and it is targeted to endosomes[20]. It is known to bind integrins and inhibit cellular migration through a Rac1–Pak1 signaling pathway[21]. We asked whether the upregulation of Nischarin in the Marble mouse perturbs Pak1 activation by performing western blot analysis for the phosphorylated active (T422) form of Pak1 on P0 hippocampal lysates. This experiment revealed a significant reduction in the amount of activated Pak1 in *Mbe/Mbe* mutants in comparison to controls ($n = 3$, $P = 0.01$; Fig. 3g,h). Taken together, these data show that the *Mbe/Mbe* mutation alters protein homeostasis within the developing hippocampus, perturbing Nischarin–Pak1 signaling.

***Mbe/Mbe* mutants have a severe defect in hippocampal neuronal migration and working memory.** Next, we undertook a detailed examination of the neuroanatomical features of the Marble line, focusing on the hippocampus (Fig. 4a–i). Staining with the postmitotic neuronal marker NeuN and the calcium binding protein calbindin showed that the ectopic cells displaced in the stratum oriens layer of the hippocampus are excitatory pyramidal neurons (Fig. 4d–i)[22]. These ectopic clusters of neurons were most prominent in the CA1 subfield (Fig. 4a–c). Notably, immunostaining in *Mbe/Mbe* mutants revealed an enrichment of Nischarin in ectopic pyramidal cells compared with those cells that were correctly positioned (Supplementary Fig. 3c–g). Staining with calretinin and parvalbumin showed that the distribution of interneurons within the oriens layer and pyramidal cell layer is not altered in *Mbe/Mbe* animals (Supplementary Fig. 4a–n). Golgi staining revealed no difference in spine density when comparing control (+/+) and *Mbe/Mbe* pyramidal neurons (Supplementary Fig. 4o,p). In contrast, a Sholl analysis highlighted a significant decrease in dendritic complexity in ectopic CA1 pyramidal cell neurons in *Mbe/Mbe* mutants that was not evident in correctly positioned neurons in *Mbe/Mbe* mutants or wild-type littermates ($n = 3$ animals per genotype, $P < 0.0001$; Supplementary Fig. 4q,r). Staining of the dentate gyrus with sera against GFAP (which labels glial-like progenitors), Tbr2 (which labels intermediate progenitors), Dcx (which labels newly born neurons) and Prox1 (which labels granule cells) revealed that the organization of the subgranular zone and granule cell layer is not affected in *Mbe/Mbe* mutants ($n = 3$; Supplementary Fig. 5a–x). To investigate the origin of the fractured pyramidal cell layer in *Mbe/Mbe* mutants, we performed birthdate labeling, injecting BrdU at E14.5, a peak time for hippocampal neurogenesis, and killed the mice and collected their brains at P11 ($n = 3$). Blind quantitation revealed a significantly higher percentage of BrdU+ cells in the stratum oriens in mutant animals (15.2% ± 1.2%) in comparison to littermate controls (10.4% ± 0.1%; $n = 3$, $P = 0.0002$). This was accompanied by a concomitant decrease in BrdU+ cells in the pyramidal cell layer in *Mbe/Mbe* animals ($n = 3$; +/+: 59.6% ± 0.5%, *Mbe/Mbe*: 54.5% ± 1%, $P < 0.0001$; Fig. 4j,k). To assess whether ectopic neurons in the pyramidal cell layer are generated during a broader time window, we performed additional BrdU labeling at E12.5 and E16.5, quantifying the percentage of ectopic BrdU+NeuN+ cells ($n = 3$). This experiment showed that the neurons that form the ectopic layer are born at E12.5, E14.5 and E16.5 (Fig. 4l–w).

Next, we asked whether perturbation of Vps15 in neurons is sufficient to cause a fractured pyramidal cell layer in the hippocampus by exploiting a *Vps15*–conditional knockout mouse[23]. As adult homozygous knockout (*loxP*-flanked; hereafter *fl*) animals are not viable, we intercrossed the conditional-knockout line with *Mbe/Mbe* mutants, generating compound heterozygotes (*fl/Mbe*). In the absence of a Cre-recombinase, we observed normal lamination in the hippocampus (Fig. 4x,aa). We then performed genetic crosses, introducing either Emx1-Cre (which is expressed in both neurons and radial glia in the forebrain from E10.5)[24] or Nex-Cre (which is only expressed in postmitotic neurons in the cortex and hippocampus from E11.5)[25]. Both the *fl/Mbe* Nex-Cre and *fl/Mbe* Emx1-Cre lines recapitulated the fractured pyramidal cell layer we observed in *Mbe/Mbe* mutants, with an increase in the number of ectopic pyramidal cells (Fig. 4y,ab). The numbers of ectopic cells in the oriens layer were similar in *fl/Mbe* Emx1-Cre (31% ± 4.5%, $n = 3$) and *fl/Mbe* Nex-Cre (38% ± 3%, $n = 2$) animals (Fig. 4z,ac). These data indicate that the fractured pyramidal cell layer we observed in the *Mbe/Mbe* hippocampus is attributable to Vps15 perturbation in neurons and not to glial dysfunction.

Given the defects in hippocampal lamination in the *Mbe/Mbe* mice we assessed their performance on a memory task that is hippocampal dependent. Employing rewarded alternation in the T-maze, we found that *Mbe/Mbe* mutants alternated just above
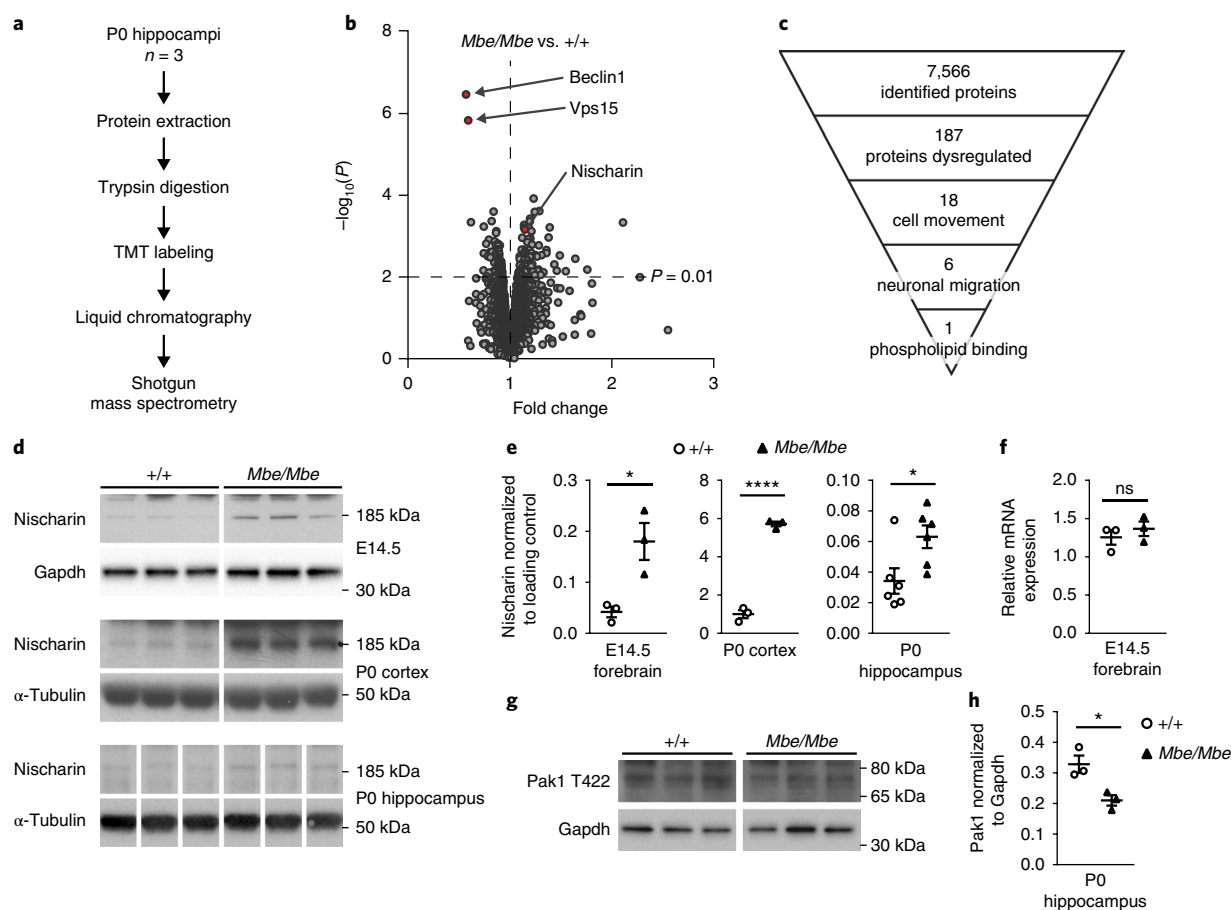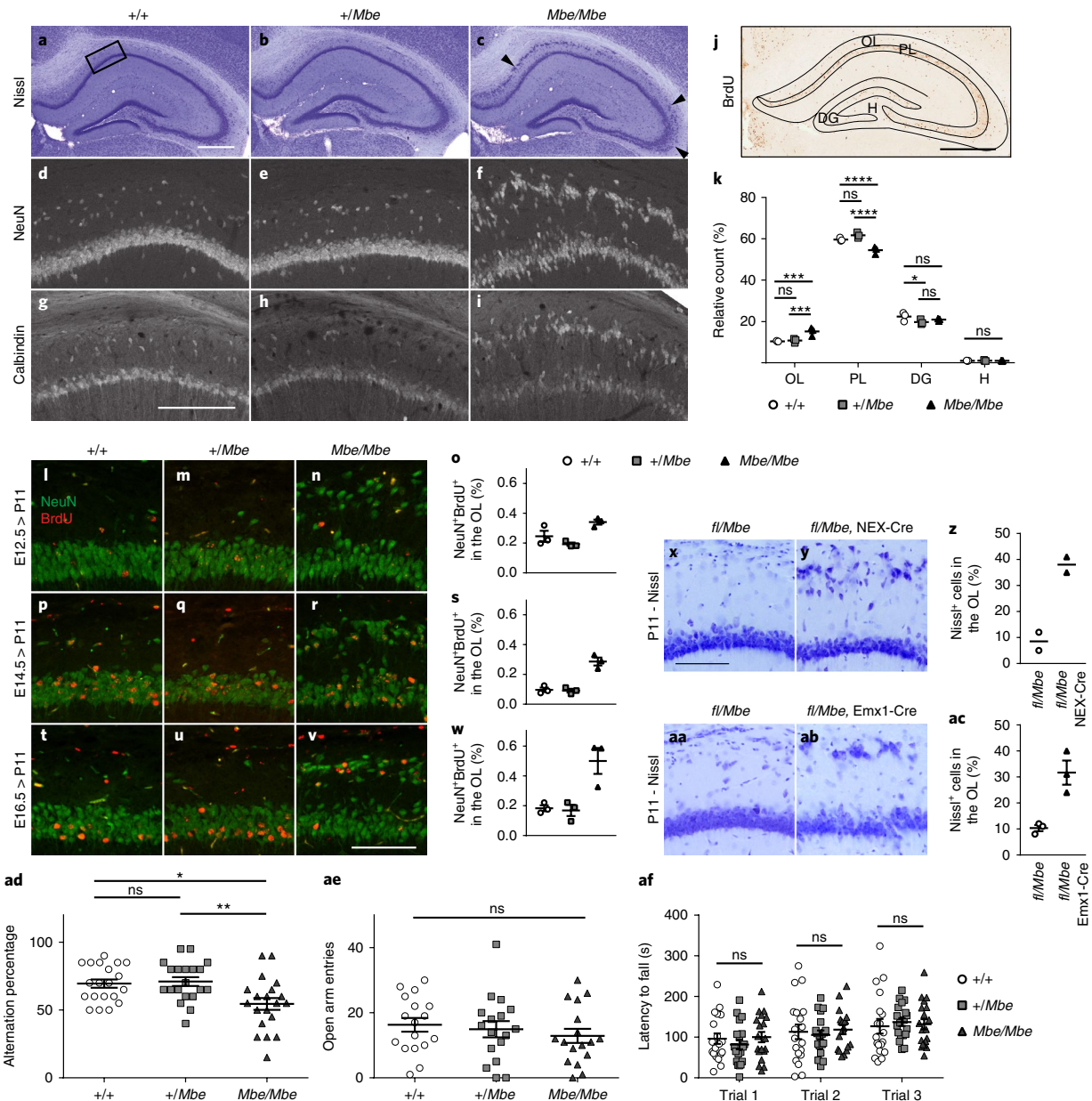
Fig. 3 | Global quantitative proteomics reveals that Nischarin is upregulated in *Mbe/Mbe* mutants. a, Schematic depicting the methodology employed for proteomic experiments. Hippocampi from *Mbe/Mbe* mutants and wild-type controls at P0 ($n = 3$ biological replicates per genotype, each consisting of pooled hippocampi from 2 animals) were lysed, and proteins extracted and subjected to tryptic digest before tandem mass tag (TMT) labeling. Following separation of protein fragments by liquid chromatography, samples were analyzed by mass spectrometry. **b**, Volcano plot showing peptides upregulated and downregulated in the *Mbe/Mbe* hippocampus with $-\log_{10}(P)$ values shown on the y axis, following the application of a modified t test with Bayesian parameters. **c**, Pyramid showing how mass spectrometry data were analyzed. **d,e**, Western blot analysis and quantification confirm that Nischarin protein levels are increased in the *Mbe/Mbe* developing forebrain (E14.5; $n = 3$ animals per genotype; one-tailed unpaired t test; $t_4 = 3.667$, $P = 0.01$), P0 cortex ($n = 3$ animals per genotype; one-tailed unpaired t test; $t_4 = 19.19$, $P < 0.0001$) and P0 hippocampus ($n = 6$ animals per genotype; one-tailed unpaired t test; $t_{10} = 2.584$, $P = 0.01$). This experiment was performed twice with similar results. **f**, Quantification of mRNA expression of Nischarin in the E14.5 forebrain reveals no differences between genotypes ($n = 3$ animals per genotype; Mann–Whitney test, two tailed; $P = 0.4$). **g**, Western blot analysis of activated Pak1 (phosphorylated at T422) shows decreased Pak1 activation in the *Mbe/Mbe* P0 hippocampus. This experiment was performed twice with similar results. **h**, Quantification of Pak1 western blot reveals that the difference between genotypes is significant ($n = 3$ animals per genotype; one-tailed unpaired t test; $t_4 = 3.597$, $P = 0.01$). *$P < 0.05$; ****$P < 0.0001$; ns, not significant. All immunoblots shown are cropped; see Supplementary Fig. 11 for full-length blots. Error bars show mean ± s.e.m.

chance (54% ± 4%), in contrast to heterozygotes (71% ± 3%) and +/+ (70% ± 3%) littermates (Fig. 4ad, $n = 20$, *Mbe/Mbe* vs. +/+: $P = 0.01$). An assessment of their anxiety-related behaviors employing the elevated-plus maze and open field revealed that *Mbe/Mbe* mutants are indistinguishable from wild-type controls (open arm entries, $n = 17$; *Mbe/Mbe* vs. +/+, $P = 0.54$; Fig. 4ae and Supplementary Fig. 5y,z). Similarly, they exhibit no defects in motor coordination when assessed with the rotarod ($n = 19$; *Mbe/Mbe* vs. +/+, $P = 0.85$; Fig. 4af). Taken together, these data show that the primary behavioral deficit in *Mbe/Mbe* mutants is working spatial memory, which is associated with a fractured pyramidal cell layer in the hippocampus.

***Mbe/Mbe* mutants have a mild defect in cortical neuronal migration.**
We investigated whether the laminar architecture of the cortex is also affected in *Mbe/Mbe* mutants by staining with sera against NeuN, Cux1 (a layer II/III and IV marker), Er81 (a layer V marker)

and Foxp2 (a layer VI marker; $n = 3$; Fig. 5a–l). Using these antibodies, we were not able to detect any differences when comparing wild-type controls and *Mbe/Mbe* mutants, indicating that the structure of the cortex is intact in mutant animals. Next, we assessed neuronal migration in the cortex by birthdate-labeling experiments at E12.5, E14.5 and E16.5, after which mice were killed for analysis (blind quantitation) at P0. We divided the cortex into ten equal bins and counted the number of BrdU+ cells in each bin. We observed a mild migratory defect in *Mbe/Mbe* animals that was most noticeable following injection at E16.5. At this timepoint there was a significant accumulation of BrdU+ neurons in bins 9 and 10, with a concomitant decrease in bin 8 in *Mbe/Mbe* mutants ($n = 3$, +/+ vs. *Mbe/Mbe*; bin 8: $P = 0.01$; bin 9: $P = 0.02$; bin 10: $P = 0.002$). Moreover, there was a significant interaction between genotype and the distribution of BrdU+ cells across all bins ($n = 3$, $P = 0.02$; Fig. 5m–p and Supplementary Fig. 6a–h). Quantification of cortical thickness revealed no significant differences between *Mbe/Mbe*
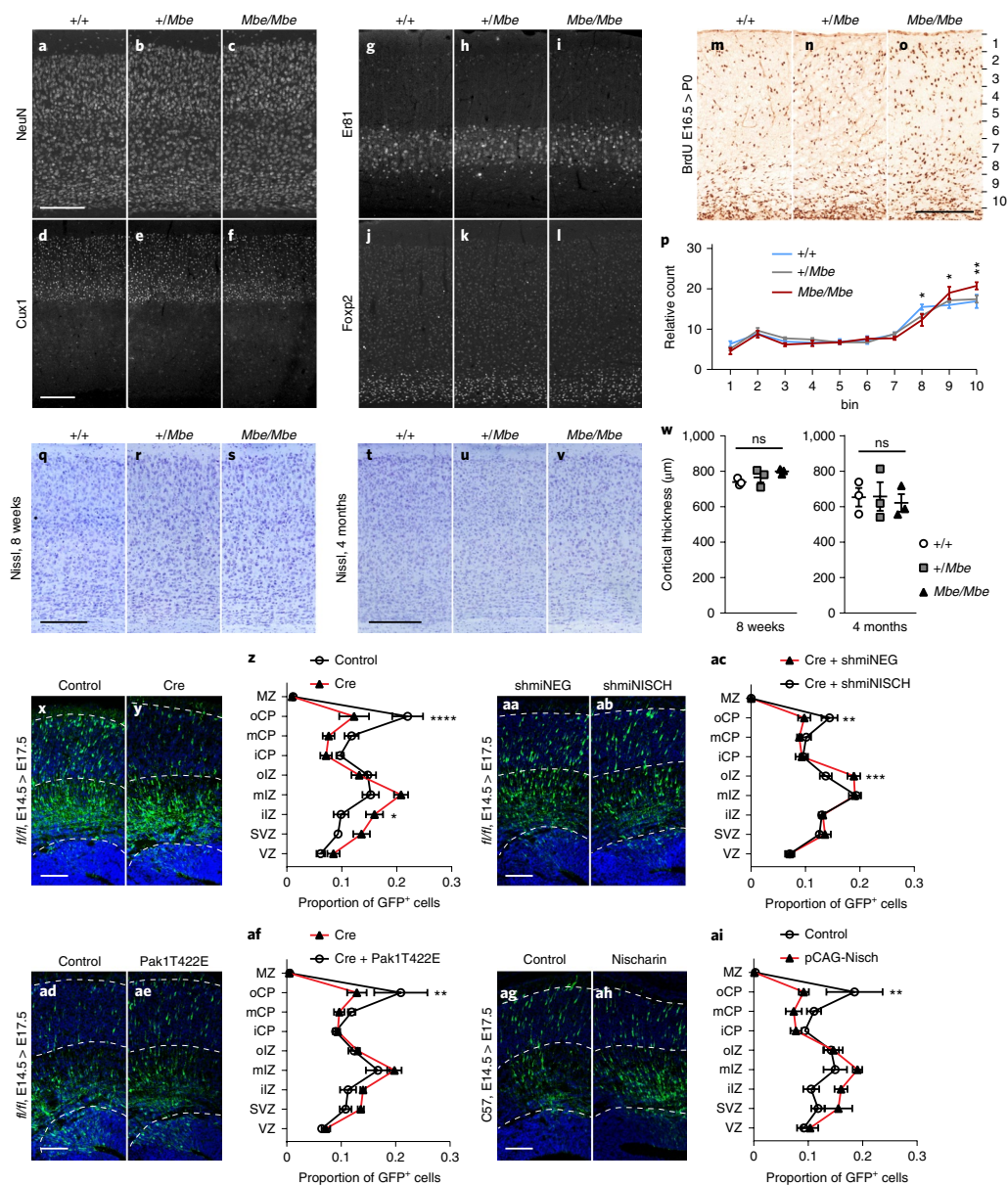
Fig. 4 | Neuroanatomical characterization of the *Mbe/Mbe* hippocampus. a–c, Representative Nissl stains of the hippocampus of wild-type controls (+/+), heterozygotes (+/*Mbe*) and Marble mutants (*Mbe/Mbe*) aged 8 weeks (*n* = 3 animals per genotype). Arrowheads highlight the fractured pyramidal cell layer visible in *Mbe/Mbe* mutants, which is most severe in the CA1 subfield but extends into CA2 and CA3. **d–i,** NeuN (**d–f**) and calbindin (**g–i**) staining of area boxed in **a** confirms that ectopic cells are pyramidal neurons. These experiments were performed twice with similar results. **j,** Diagram showing the regions of the hippocampus analyzed following BrdU injections at E14.5 and brain collection at P11. **k,** Graph showing the percentage of BrdU+ cells in the oriens layer (OL), pyramidal cell layer (PL), dentate gyrus (DG) and hilus (H). In *Mbe/Mbe* mutants we observe a significant increase in the percentage of BrdU positive cells in OL (*n* = 3 animals per genotype; two-way repeated-measures ANOVA with Tukey's test for multiple comparison; +/+ vs. *Mbe/Mbe*, *P* = 0.0002; +/*Mbe* vs. *Mbe/Mbe*, *P* = 0.005) with a concomitant decrease in PL (+/+ vs. *Mbe/Mbe*, *P* < 0.0001; +/*Mbe* vs. *Mbe/Mbe*, *P* < 0.0001). **l–w,** Representative images of the pyramidal cell layer following BrdU injection at E12.5 (**l–n**), E14.5 (**p–r**) and E16.5 (**t–v**), stained with sera against NeuN (green) and BrdU (red). (**o,s,w**) Quantifications of the percentages of ectopic NeuN+BrdU+ neurons in OL relative to the total number of NeuN+BrdU+ neurons in CA1 in +/+, +/*Mbe* and *Mbe/Mbe* animals. Neurons destined for the OL in *Mbe/Mbe* mutants are born at E12.5, E14.5 and E16.5. **x–ac,** Generation of *fl/Mbe* compound heterozygotes in the absence of a Cre driver line (**x,aa**), or alternatively with a Nex-Cre (**y**) or Emx1-Cre (**ab**) driver. Representative images of the CA1 region of the hippocampus are shown. No lamination defect is apparent in the absence of Cre (**x,aa**), whereas ablation of Vps15 by Emx1-Cre or Nex-Cre recapitulates the *Mbe/Mbe* phenotype (**y,ab**). (**z,ac**) Quantitation of ectopic pyramidal cells in *fl/Mbe* Nex-Cre (38% ± 4%, *n* = 2 animals per genotype) and *fl/Mbe* Emx1-Cre mice (31% ± 8%, *n* = 3 animals per genotype). **ad–af,** *Mbe/Mbe* mutants exhibit a defect in working spatial memory (**ad**) when assessed using rewarded alternation (*n* = 20 animals per genotype; one-way ANOVA with Tukey's multiple comparison; +/+ vs. *Mbe/Mbe*, *P* = 0.013; +/*Mbe* vs. *Mbe/Mbe*, *P* = 0.006) but normal anxiety phenotypes on the elevated plus maze (**ae,** open arm entries; *n* = 17 animals per genotype; one-way ANOVA with Tukey's multiple comparison; +/+ vs. *Mbe/Mbe*, *P* = 0.54) and normal motor coordination on the rotarod (**af,** *n* = 19 animals per genotype; two-way repeated-measures ANOVA with Tukey's multiple-comparison test; +/+ vs. *Mbe/Mbe* trial 1: *P* = 0.98; trial 2: *P* = 0.95; trial 3: *P* = 0.97). Scale bars: in **a** and **j**, 500 μm; in **g**, 200 μm; in **v** and **x**, 100 μm. **P* < 0.05; ***P* < 0.01; ****P* < 0.001; *****P* < 0.0001; ns, not significant. Error bars show mean ± s.e.m.

Fig. 5 | Cortical architecture is preserved in *Mbe/Mbe* mutants, but acute depletion of *Vps15* results in a neuronal migration defect. a–l, Representative immunostaining of the cortex for +/+, +/*Mbe* and *Mbe/Mbe* animals aged 8 weeks, using NeuN (**a–c**), Cux1, which labels layers II–IV (**d–f**), Er81, which labels layer V (**g–i**), and Foxp2, which labels layer VI (**j–l**; *n* = 3 animals per genotype). Cortical lamination is preserved in *Mbe/Mbe* mutants. These experiments were performed twice with similar results. **m–p**, Birthdate labeling results, showing representative coronal sections stained with sera against BrdU. BrdU was delivered to pregnant dams at E16.5, followed by analysis of brains at P0. The cortex was divided into ten equal bins and the distribution of BrdU+ cells mapped for +/+, +/*Mbe* and *Mbe/Mbe* animals (*n* = 3 animals per genotype). There was a significant interaction effect between genotype and distribution of cells across all bins (*n* = 3 animals per genotype; two-way repeated-measures ANOVA with Tukey's multiple-correction test; $F_{18,54} = 2.081$, *P* = 0.02). In addition, there was a significant accumulation of BrdU+ neurons in bins 9 (+/+ vs. *Mbe/Mbe*, *P* = 0.018) and 10 (+/+ vs. *Mbe/Mbe*, *P* = 0.002; +/*Mbe* vs. *Mbe/Mbe*, *P* = 0.008), with a concomitant reduction of BrdU+ neurons in bin 8 (+/+ vs. *Mbe/Mbe*, *P* = 0.01). **q–v**, Representative Nissl staining of the somatosensory cortex of +/+, +/*Mbe* and *Mbe/Mbe* animals aged 8 weeks (**q–s**) and 4 months (**t–v**). **w**, Quantification of cortical thickness reveals no significant difference between genotypes (*n* = 3 animals per genotype; one-way ANOVA with Tukey's multiple comparison; 8 weeks: +/+ vs. *Mbe/Mbe*, *P* = 0.13; +/*Mbe* vs. *Mbe/Mbe*, *P* = 0.44; 4 months: +/+ vs. *Mbe/Mbe*, *P* = 0.93; +/*Mbe* vs. *Mbe/Mbe*, *P* = 0.91). **x–ai**, Representative images for in utero electroporation experiments. Constructs were electroporated at E14.5 before analysis at E17.5. (**x–z**) Electroporation with a control vector or pCAG-Cre in *Vps15 fl/fl* animals revealed an accumulation of cells in the intermediate zone with a concomitant reduction in the cortical plate (*n* = 6 animals per condition; interaction *P* < 0.0001). (**aa–ac**) Expression of a shmiRNA targeting Nischarin (shmiNISH) partially rescues the phenotype caused by Cre mediated *Vps15* depletion (shmiNEG, negative control shmiRNA; *n* = 4 animals per condition; interaction *P* = 0.002). (**ad–af**) Overexpression of a phosphomimetic mutant of Pak1 (T422E) partially rescues the phenotype caused by Cre mediated *Vps15* depletion (*n* = 6 animals per condition; interaction *P* = 0.03). (**ag–ai**) Overexpression of Nischarin (pCAG-Nisch) in wild-type mice results in a defect in neuronal migration with a notable reduction in the number of GFP+ cells in the cortical plate (*n* = 4 animals per condition; interaction *P* = 0.01). VZ, ventricular zone; SVZ, subventricular zone; IZ, intermediate zone; CP, cortical plate; MZ, marginal zone; oCP, mCP, iCP, oIZ, mIZ and iIZ, outer, inner and medial CP and IZ, respectively. For **x–ai** we used two-way repeated-measures ANOVA with Bonferroni multiple-comparison tests; see Supplementary Table 1. **P* << 0.01; ****P* < 0.001; *****P* < 0.0001. Scale bars in **a**, **d**, **o**, **q** and **t**: 200 μm; in **x**, **aa**, **ad** and **ag**: 100 μm. Error bars show mean ± s.e.m.

mutants and littermate controls at 8 weeks of age ($n=3$; +/+ vs. *Mbe/Mbe*, $P=0.13$) or 4 months ($n=3$; +/+ vs. *Mbe/Mbe*, $P=0.93$; Fig. 5q–w). Analysis of the laminar structure of the cerebellum, employing markers such as Foxp2 and calbindin, revealed no differences between genotypes (Supplementary Fig. 6i–q).

Acute depletion of Vps15 causes neuronal migration defects in the murine cortex. As the *Mbe/Mbe* mutation results in some functional protein, we explored the effect of acute depletion of Vps15 in the developing cortex. We performed in utero electroporation on *Vps15*-knockout animals at E14.5, delivering a Cre recombinase alongside a GFP-expressing vector. Animals were killed for analysis at E17.5, and the distribution of GFP+ cells was blindly quantitated. We found that acute depletion of Vps15 results in a severe migration defect, with a notable reduction of GFP+ cells in the outer cortical plate (oCP; $n=6$, $P<0.0001$; Fig. 5x–z). Given that Nischarin is found at higher levels in *Mbe/Mbe* mutants, we then asked whether Nischarin knockdown might rescue the aforementioned migration defect. First, we confirmed that knockdown of Nischarin, by itself, does not influence neuronal migration, by delivering short hairpin microRNAs (shmiRNAs) validated in Neuro2A cells to the developing cortex (Supplementary Fig. 7a–e). Next, we delivered a Cre recombinase to Vps15–conditional knockout animals at E14.5 with shmiRNAs targeted to Nischarin or, alternatively, a scrambled control. Blind quantitation showed that Nischarin knockdown partially

rescued the cortical migration defect that results from acute Vps15 depletion ($n=4$, $P=0.003$, oCP; Fig. 5aa–ac). Given the decreased phosphorylation (T422) of the downstream Nischarin effector Pak1 in *Mbe/Mbe* mutants, we then asked whether the effect of acute Vps15 ablation could be alleviated by expression of a Pak1 phosphomimetic. While overexpression of T422E Pak1 itself does not significantly influence the distribution of neurons ($n=4$ animals per condition, interaction $P=0.7074$; Supplementary Fig. 7f–h), when delivered with a Cre recombinase on the Vps15-knockout background, it enhanced neuronal migration ($n=6$, $P=0.003$, oCP; Fig. 5ad–af). We further predicted that overexpression of Nischarin would cause a severe defect in migration in wild-type animals. To test this, we performed in utero electroporation of wild-type C57/Bl6J mice, which were killed for analysis at E17.5. Blind quantitation revealed an increase in the number of GFP+ cells in the subventricular and ventricular zones in animals overexpressing Nischarin, with a concomitant reduction in oCP ($n=4$, $P=0.005$; Fig. 5ag–ai and Supplementary Fig. 7i–n). Taken together, these experiments support the hypothesis that neuronal migration defects caused by Vps15 depletion are associated with perturbation of a Nischarin–Pak1 signaling pathway.

Complete ablation of Vps15 causes severe cortical atrophy. Next, we explored the impact of a complete ablation of Vps15 in the telencephalon, using a Vps15–conditional knockout animal crossed
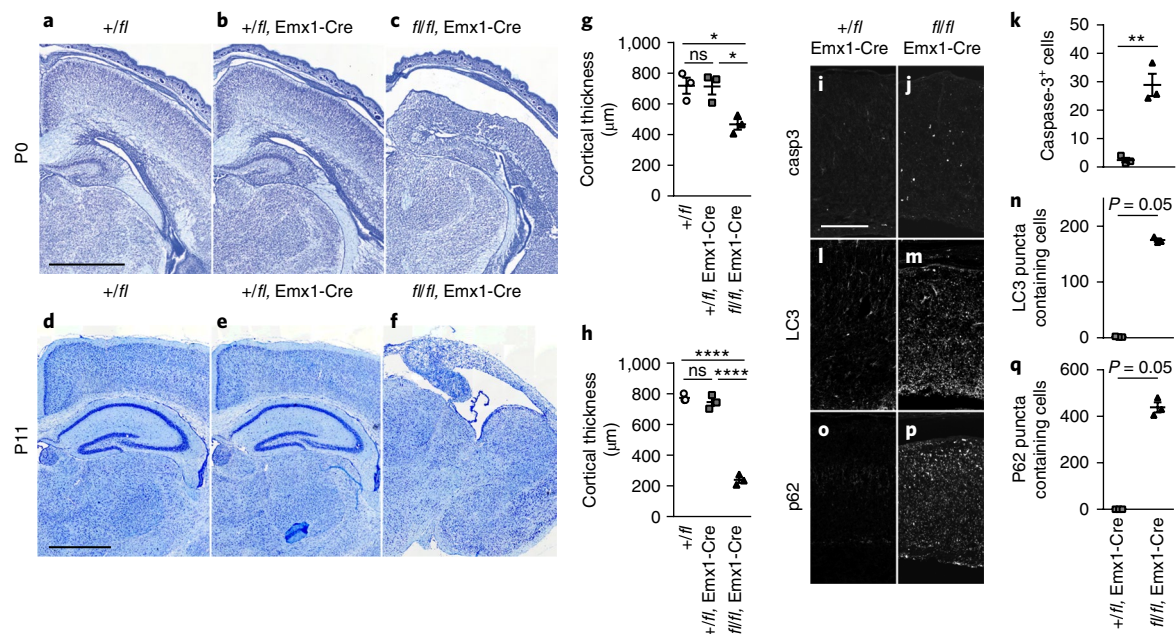

Fig. 6 | Severe cortical atrophy and caspase-induced apoptosis in Vps15-knockout animals. a–f, Representative Nissl stains of Vps15-knockout animals crossed with the Emx1-Cre driver line at P0 (**a–c**) or P11 (**d–f**). Three genotypes are shown; controls without Cre (+/*fl*), heterozygotes with Cre (+/*fl* Emx1-Cre) and homozygotes with Cre (*fl/fl* Emx1-Cre). While heterozygotes are unaffected, homozygous animals present with cortical atrophy at P0 that is more severe at P11, indicative of a progressive phenotype. These experiments were performed twice with similar results. **g,h**, Quantification at P0 (**g**) and P11 (**h**) reveals a highly significant reduction in cortical thickness in homozygous (*fl/fl* Emx1-Cre) animals (P0: $n=3$ animals per genotype; one-way ANOVA with Tukey's multiple comparison; +/*fl* vs. *fl/fl* Emx1-Cre, $P=0.026$; +/*fl* Emx1-Cre vs. *fl/fl* Emx1-Cre, $P=0.028$; P11: $n=3$ animals per genotype; one-way ANOVA with Tukey's multiple comparison; +/*fl* vs. *fl/fl* Emx1-Cre, $P<0.0001$; +/*fl* Emx1-Cre vs. *fl/fl* Emx1-Cre, $P<0.0001$). **i,j**, Representative images of caspase3 stained of P0 cortices in +/*fl* Emx1-Cre animals (which serve as controls as no phenotype is evident) and *fl/fl* Emx1-Cre mice ($n=3$ animals per genotype). **k**, Quantification of caspase-3 staining shows a highly significant increase in positive cells in *fl/fl* Emx1-Cre mutants ($n=3$ animals per genotype; one-tailed unpaired t test, $t_4=6.62$, $P=0.001$). **l,m**, LC3 staining in P0 cortices (representative images) reveals the presence of LC3 aggregations in *fl/fl* Emx1-Cre animals. **n**, Quantification of LC3 puncta in +/*fl* Emx1-Cre and *fl/fl* Emx1-Cre mice reveals a significant difference between genotypes ($n=3$ animals per genotype; Mann–Whitney test, one-tailed; $P=0.05$). **o–q**, p62 staining in P0 cortices (representative images) shows an upregulation of this cargo receptor in *fl/fl* Emx1-Cre that is significant and indicative of defects in the clearance of autophagosomes ($n=3$ animals per genotype; Mann–Whitney test, one-tailed; $P=0.05$). Scale bars in **a** and **d**, 1,000 μm; in **i**, 200 μm. *$P<0.05$; **$P<0.01$; ****$P<0.0001$. Error bars show mean ± s.e.m.
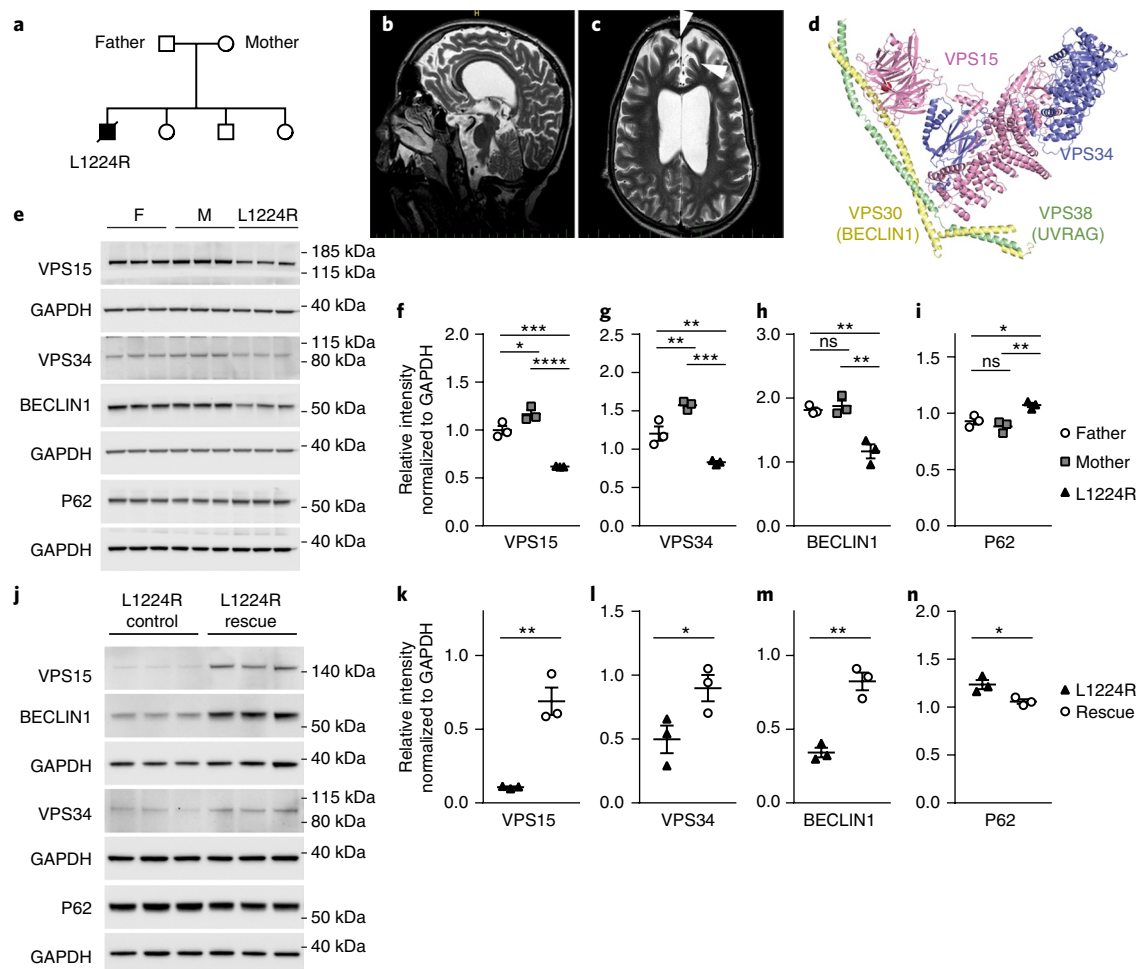
Fig. 7 | An L1224R mutation in *VPS15* is associated with neurodevelopmental disease. a, Structure of the family harboring a missense mutation in *VPS15*. The father and mother are heterozygous for the variant, whereas the proband (filled box) is homozygous for the L1224R mutation. Unaffected siblings were either heterozygous or wild-type. **b,c,** MRI images of the affected patient (at age 16) who presents with bilateral cortical and optic nerve atrophy, regions of cortical dysplasia (arrowheads), ataxia, intellectual impairment and epilepsy. **d,** Structural model of the VPS15–VPS34–BECLIN1 complex, with VPS15 shown in pink. The L1224R mutation lies in the WD40 domain in the fourth beta strand and is part of a hydrophobic core (red dot). **e,** Western blot analysis of VPS15, VPS34, BECLIN1 and P62 in protein lysates from dermal fibroblasts obtained from the father (F), mother (M) and proband (L1224R). **f–i,** Normalization with GAPDH reveals a highly significant reductions in VPS15, VPS34 and BECLIN1 in the affected proband and mild reductions in VPS15 and VPS34 in the father ($n = 3$ separate flasks per individual, one-way ANOVA with Tukey's multiple comparison; VPS15: father vs. mother, $P = 0.036$; father vs. proband, $P = 0.0007$; mother vs. proband, $P < 0.0001$; VPS34: father vs. mother, $P = 0.01$; father vs. proband, $P = 0.009$; mother vs. proband, $P = 0.0002$; BECLIN1: father vs. proband, $P = 0.004$; mother vs. proband, $P = 0.0052$; P62: father vs. proband, $P = 0.02$; mother vs. proband, $P = 0.006$). These experiments were performed twice with similar results. **j,** Western blot analysis of lentiviral rescue experiment. L1224R fibroblasts were infected with a lentivirus expressing either mCherry (control), or mCherry + wild-type VPS15 (rescue). **k–m,** This resulted in significant increases in VPS15, VPS34 and BECLIN1 in the rescue cells ($n = 3$ separate flasks per individual, one-tailed unpaired t test; VPS15: $P = 0.002$; VPS34: $P = 0.03$; BECLIN1: $P = 0.001$). These experiments were performed twice with similar results. **n,** Ectopic expression of VPS15 in L1224R cells resulted in a significant reduction in P62 ($n = 3$ separate flasks per individual, one-tailed unpaired t test, $P = 0.015$). All immunoblots shown are cropped; see Supplementary Fig. 11 for full-length blots. Error bars show mean ± s.e.m. *$P < 0.05$; **$P < 0.01$; ***$P < 0.001$; ****$P < 0.0001$.

to the Emx1-Cre driver line[23]. We did not observe a phenotype in heterozygous animals (+/*fl* Emx1-Cre) but noted a reduction in cortical thickness in homozygotes (*fl/fl* Emx1-Cre) at P0 that was more severe at P11 (Fig. 6a–h). At both timepoints the hippocampus was barely discernible, with no structured pyramidal cell layer or dentate gyrus. This degeneration was accompanied by a large increase in caspase-3+ apoptotic cells in *fl/fl* Emx1-Cre animals at P0 (Fig. 6i–k). This phenotype was also evident at E14.5, where we again observed a reduction in cortical thickness, with extensive apoptosis in proliferative and postmitotic regions (Supplementary Fig. 8a–g). At E14.5 we observed a reduction in the thickness of Sox2+ and Tbr2+ progenitors, a decrease in the mitotic output as assessed by pH3 staining and a disorganized radial glial scaffold in

fl/fl Emx1-Cre animals (Supplementary Fig. 8h–s). Next, we undertook histological analysis of P0 cortical sections stained with sera against LC3 and p62, which serves a cargo receptor for the autophagic degradation of ubiquitinated substrates[26]. We observed a large increase in the number of cells with p62+ (Fig. 6o–q) and LC3+ (Fig. 6l–n) puncta. Taken together, these data show that complete ablation of Vps15 results in severe, progressive degeneration of the hippocampus and cortex that is associated with caspase-induced apoptosis and the accumulation of LC3+ and p62+ substrates.

Mutations in *VPS15* are associated with neurodevelopmental disease in humans. Given that the *Mbe/Mbe* mice present with defects in neuronal migration and that complete ablation of Vps15

results in severe cortical atrophy, we explored whether mutations in the human homolog would result in structural brain phenotypes. We networked with clinical geneticists through interfaces such as Genematcher[27]. This resulted in the identification of a family with non-consanguineous parents in which one of four children presented with severe cortical and optic nerve atrophy, localized cortical dysplasia, intellectual impairment, spasticity, ataxia, psychomotor delay, muscle wasting, pseudobulbar palsy, a mild hearing deficit and late-onset epilepsy (Fig. 7a–c). Whole-exome sequencing (WES) of all family members identified a single homozygous coding variant in the affected patient that was not reported in online genome databases (for example, ExAC genome browser). We did not identify any other unreported de novo or inherited variants in the affected patient. This variant, an A-to-C mutation in *VPS15* (GRCh38.p5; chr3: 130,681,528), alters a highly conserved leucine residue to arginine (L1224R) (Supplementary Fig. 9a,b). One unaffected sibling and both unaffected parents are heterozygous for this variant. We mapped the position of the mutation onto the structure of the yeast Vps15–Vps34–Beclin1 complex. L1224 lies within the WD40 domain of Vps15 on the fourth beta strand, a blade that is important for folding and stability[28] (Fig. 7d).

We hypothesized that the L1224R mutation might compromise the stability of this protein complex. To test this, we obtained dermal fibroblasts from the affected individual and his parents. Western blot analysis revealed a large reduction in the amount of VPS15 protein in the proband in comparison to parental fibroblasts ($n = 3$ replicates, proband vs. mother: $P < 0.0001$; proband vs. father: $P = 0.0007$; Fig. 7e,f). We also observed a concomitant decrease in the levels of VPS34 and BECLIN1 in fibroblasts of the affected patient ($n = 3$ replicates, VPS34: proband vs. mother, $P = 0.0002$; proband vs. father, $P = 0.009$; BECLIN1: proband vs. mother, $P = 0.002$; proband vs. father, $P = 0.004$; Fig. 7e,g,h). In general, we observed reduced levels of the VPS15–BECLIN1–VPS34 complex in the father in comparison to the mother. We did not observe any significant differences in mRNA levels for VPS15, VPS34 and BECLIN1 when comparing patient and parent cell lines, indicating that the reduction in protein levels is due to post-transcriptional dysregulation (Supplementary Fig. 9c). An assessment of the number of autophagosomes and autophagy flux by analysis of LC3-I and LC3-II levels revealed a mild impairment in the patient when compared to his parents, but this difference was not statistically significant (Supplementary Fig. 9d–g). In contrast, we did observe a significant increase in the levels of the autophagy cargo receptor P62 ($n = 3$, proband vs. mother: $P = 0.006$; proband vs. father: $P = 0.02$; Fig. 7e,i) and a reduction in LysoTracker staining in the cells of the proband when compared to the father ($n = 3$, proband vs. father: $P = 0.046$; Supplementary Fig. 9h,i).

We asked whether we could rescue the accumulation of P62+ autophagic substrates in the L1224R patient cells by ectopically expressing wild-type VPS15. To do so, we generated a lentivirus that expresses VPS15 and mCherry. Delivery of this virus to patient cells resulted in upregulation of the VPS15 protein and stabilization of BECLIN1 and VPS34 levels (Fig. 7j–m). Moreover, in comparison to infected control cells, we observed a significant decrease in P62 levels upon ectopic expression of VPS15 ($n = 3$, $P = 0.015$; Fig. 7j,n). Taken together, these data show that the L1224R mutation compromises the function of the VPS15–BECLIN1–VPS34 complex, leads to an accumulation of autophagic substrates and indicates that mutations in VPS15 are associated with human neurodevelopmental disease.

Discussion

The role of Vps15 in neuronal migration. Here we report the establishment of a forward genetics screen for mice with structural brain phenotypes. This has resulted in the identification of the Marble mouse, which presents with a fractured pyramidal cell layer in the hippocampus, attributable to an impairment in neuronal migration and a hypomorphic mutation in *Vps15*. How do mutations in Vps15 cause defects in neuronal migration? We have shown that there is a large increase in Nischarin in the developing telencephalon in *Mbe/Mbe* mutants, accompanied by reduction in activated Pak1. This result is consistent with previous studies showing that Nischarin binds to and inhibits the kinase activity of Pak1, exerting an inhibitory impact on cell migration[21]. This is further reinforced by our in utero electroporations, which showed that acute ablation of Vps15 in the cortex results in a migration defect that can be rescued, in part, by reducing the levels of Nischarin or by overexpression of a Pak1 phosphomimetic. Pak1 is known to play a critical role in cytoskeletal organization, by influencing microtubule dynamics through the phosphorylation of tubulin cofactor B[29]. Pak1 has also been reported to influence the actin cytoskeleton by activating LIM kinase (LIMK1), which regulates cofilin phosphorylation[30]. There is further evidence that the amino terminus of Nischarin binds directly to the PDZ domains of LIMK1, exerting an inhibitory effect[31]. Cofilin phosphorylation has been shown to stabilize the actin cytoskeleton in the leading process of migrating neurons, promoting somal translocation[32]. The reduced levels of activated Pak1 in *Mbe/Mbe* mutants and the abundance of Nischarin might result in decreased cofilin phosphorylation, destabilizing the leading process. As Nischarin is known to bind integrins, it is also conceivable that the distribution of cell surface receptors may be altered in *Mbe/Mbe* mutants. Anton and colleagues have shown that perturbation of integrin signaling in α3β10-deficient neurons results in a defect in neuronal migration that is associated with altered actin dynamics in the leading and trailing processes[33]. In light of this fact, and as Nischarin and Pak1 have multiple effectors, we propose that the neuronal migration defect in *Mbe/Mbe* mutants involves multiple pathways that converge on the microtubule and actin cytoskeleton (Supplementary Fig. 10). We emphasize that we cannot exclude the possibility that other proteins misregulated in the Marble mouse (for example, Fgfr3 or Slit2) also contribute to the phenotype; however, it is apparent that overexpression of Nischarin alone is sufficient to result in a neuronal migration phenotype.

Phospholipids and neurodevelopmental disease. Evidence that abnormalities in the processing of various phospholipids cause neurodevelopmental syndromes[34] is accumulating. Genetic studies in humans have shown that mutations in PIK3R2 and PIK3CA cause a spectrum of phenotypes, including megalencephaly, polymicrogyria and focal cortical dysplasia, the last of which in some instances is accompanied by hydrocephalus and polydactyly[35,36]. Together, PIK3R2 and PIK3CA are responsible for phosphorylating phosphatidylinositol 4,5-bisphosphate, generating phosphatidylinositol 3,4,5-trisphosphate (PIP3), which regulates a wide range of cellular processes. More recently, mutations in SNX14, a protein that is associated with late endosomes and lysosomes and that binds to phosphatidylinositol (3,5)-bisphosphate, was shown to cause cerebellar atrophy. This phenotype was associated with impaired autophagic clearance and subsequent caspase-induced cell death[26]. This work suggests that mutations in the VPS15–VPS34–BECLIN1 complex may be associated with neurological disorders, both common and rare. Indeed, there is some evidence to suggest a variant within the promoter of *VPS34* may be associated with schizophrenia[37]. In summary, this work highlights the utility of forward-driven genetic screens to gain novel insights into the molecular basis of telencephalic development and underscores the importance of the Vps15–Vps34 complex in neuronal migration and survival.

Methods

Methods, including statements of data availability and any associated accession codes and references, are available at https://doi.org/10.1038/s41593-017-0053-5.

References

1. Ayala, R., Shu, T. & Tsai, L. H. Trekking across the brain: the journey of neuronal migration. *Cell* **128**, 29–43 (2007).
2. Noctor, S. C., Flint, A. C., Weissman, T. A., Dammerman, R. S. & Kriegstein, A. R. Neurons derived from radial glial cells establish radial units in neocortex. *Nature* **409**, 714–720 (2001).
3. Heng, J. I., Chariot, A. & Nguyen, L. Molecular layers underlying cytoskeletal remodelling during cortical development. *Trends Neurosci.* **33**, 38–47 (2010).
4. Gleeson, J. G. & Walsh, C. A. Neuronal migration disorders: from genetic diseases to developmental mechanisms. *Trends Neurosci.* **23**, 352–359 (2000).
5. D'Arcangelo, G. et al. A protein related to extracellular matrix proteins deleted in the mouse mutant reeler. *Nature* **374**, 719–723 (1995).
6. Sheldon, M. et al. Scrambler and yotari disrupt the disabled gene and produce a reeler-like phenotype in mice. *Nature* **389**, 730–733 (1997).
7. Keays, D. A. et al. Mutations in alpha-tubulin cause abnormal neuronal migration in mice and lissencephaly in humans. *Cell* **128**, 45–57 (2007).
8. Chae, T. et al. Mice lacking p35, a neuronal specific activator of Cdk5, display cortical lamination defects, seizures, and adult lethality. *Neuron* **18**, 29–42 (1997).
9. Dhavan, R. & Tsai, L. H. A decade of CDK5. *Nat. Rev. Mol. Cell Biol.* **2**, 749–759 (2001).
10. Keays, D. A., Clark, T. G. & Flint, J. Estimating the number of coding mutations in genotypic- and phenotypic-driven *N*-ethyl-*N*-nitrosourea (ENU) screens. *Mamm. Genome* **17**, 230–238 (2006).
11. Corbo, J. C. et al. Doublecortin is required in mice for lamination of the hippocampus but not the neocortex. *J. Neurosci.* **22**, 7548–7557 (2002).
12. Hirotsune, S. et al. Graded reduction of Pafah1b1 (Lis1) activity results in neuronal migration defects and early embryonic lethality. *Nat. Genet.* **19**, 333–339 (1998).
13. Stack, J. H., Herman, P. K., Schu, P. V. & Emr, S. D. A membrane-associated complex containing the Vps15 protein kinase and the Vps34 PI 3-kinase is essential for protein sorting to the yeast lysosome-like vacuole. *EMBO J.* **12**, 2195–2204 (1993).
14. Stein, M. P., Feng, Y., Cooper, K. L., Welford, A. M. & Wandinger-Ness, A. Human VPS34 and p150 are Rab7 interacting partners. *Traffic* **4**, 754–771 (2003).
15. Sun, Q., Westphal, W., Wong, K. N., Tan, I. & Zhong, Q. Rubicon controls endosome maturation as a Rab7 effector. *Proc. Natl. Acad. Sci. USA* **107**, 19338–19343 (2010).
16. Ruas, M. et al. TPC1 has two variant isoforms, and their removal has different effects on endo-lysosomal functions compared to loss of TPC2. *Mol. Cell Biol.* **34**, 3981–3992 (2014).
17. Tanida, I., Ueno, T. & Kominami, E. LC3 and autophagy. *Methods Mol. Biol.* **445**, 77–88 (2008).
18. Hara, T. et al. Suppression of basal autophagy in neural cells causes neurodegenerative disease in mice. *Nature* **441**, 885–889 (2006).
19. Schwämmle, V., León, I. R. & Jensen, O. N. Assessment and improvement of statistical tools for comparative proteomics analysis of sparse data sets with few experimental replicates. *J. Proteome Res.* **12**, 3874–3883 (2013).
20. Lim, K. P. & Hong, W. Human Nischarin/imidazoline receptor antisera-selected protein is targeted to the endosomes by a combined action of a PX domain and a coiled-coil region. *J. Biol. Chem.* **279**, 54770–54782 (2004).
21. Alahari, S. K., Reddig, P. J. & Juliano, R. L. The integrin-binding protein Nischarin regulates cell migration by inhibiting PAK. *EMBO J.* **23**, 2777–2788 (2004).
22. Seress, L., Gulyás, A. I. & Freund, T. F. Pyramidal neurons are immunoreactive for calbindin D28k in the CA1 subfield of the human hippocampus. *Neurosci. Lett.* **138**, 257–260 (1992).
23. Nemazanyy, I. et al. Defects of Vps15 in skeletal muscles lead to autophagic vacuolar myopathy and lysosomal disease. *EMBO Mol. Med.* **5**, 870–890 (2013).
24. Gorski, J. A. et al. Cortical excitatory neurons and glia, but not GABAergic neurons, are produced in the Emx1-expressing lineage. *J. Neurosci.* **22**, 6309–6314 (2002).
25. Goebbels, S. et al. Genetic targeting of principal neurons in neocortex and hippocampus of NEX-Cre mice. *Genesis* **44**, 611–621 (2006).
26. Akizu, N. et al. Biallelic mutations in *SNX14* cause a syndromic form of cerebellar atrophy and lysosome-autophagosome dysfunction. *Nat. Genet.* **47**, 528–534 (2015).
27. Sobreira, N., Schiettecatte, F., Valle, D. & Hamosh, A. GeneMatcher: a matching tool for connecting investigators with an interest in the same gene. *Hum. Mutat.* **36**, 928–930 (2015).
28. Rostislavleva, K. et al. Structure and flexibility of the endosomal Vps34 complex reveals the basis of its function on membranes. *Science* **350**, aac7365 (2015).
29. Vadlamudi, R. K. et al. p21-activated kinase 1 regulates microtubule dynamics by phosphorylating tubulin cofactor B. *Mol. Cell Biol.* **25**, 3726–3736 (2005).
30. Arber, S. et al. Regulation of actin dynamics through phosphorylation of cofilin by LIM-kinase. *Nature* **393**, 805–809 (1998).
31. Ding, Y., Milosavljevic, T. & Alahari, S. K. Nischarin inhibits LIM kinase to regulate cofilin phosphorylation and cell invasion. *Mol. Cell Biol.* **28**, 3742–3756 (2008).
32. Chai, X., Förster, E., Zhao, S., Bock, H. H. & Frotscher, M. Reelin stabilizes the actin cytoskeleton of neuronal processes by inducing n-cofilin phosphorylation at serine3. *J. Neurosci.* **29**, 288–299 (2009).
33. Schmid, R. S. et al. alpha3beta1 integrin modulates neuronal migration and placement during early stages of cerebral cortical development. *Development* **131**, 6023–6031 (2004).
34. Waugh, M. G. PIPs in neurological diseases. *Biochim. Biophys. Acta.* **1851**, 1066–1082 (2015).
35. Rivière, J. B. et al. De novo germline and postzygotic mutations in *AKT3, PIK3R2* and *PIK3CA* cause a spectrum of related megalencephaly syndromes. *Nat. Genet.* **44**, 934–940 (2012).
36. Mirzaa, G. M. et al. Characterisation of mutations of the phosphoinositide-3-kinase regulatory subunit, PIK3R2, in perisylvian polymicrogyria: a next-generation sequencing study. *Lancet Neurol.* **14**, 1182–1195 (2015).
37. Stopkova, P. et al. Identification of PIK3C3 promoter variant associated with bipolar disorder and schizophrenia. *Biol. Psychiatry* **55**, 981–988 (2004).

Author contributions

A.E., J.F. and D.A.K. performed the phenotypic screen and genetic mapping. T.M.K. and D.J.A. did the whole-exome sequencing on the Marble mouse. T.G., G.R. and T.Hochstoeger analyzed the expression of Vps15. T.G., I.L., M.B., S.P.-C., A.H.H., R.T. and L.L. were responsible for the characterization of the Marble and KO mouse lines. K.M. and G.D. undertook the mass spectroscopy experiments. M.R. and T.G. performed the in utero electroporation analysis. A.P., T.Honzik, M.G., S.B., E.S., S.K., V.S. and I.G. collated the clinical data and performed whole-exome sequencing and analysis of the L1224R patient. T.G. performed the functional experiments. A.K.T., T.G. and J.Z. designed and performed the lentiviral rescue experiment. T.G. and D.A.K. wrote the manuscript and all authors commented on it.

Competing interests

The authors declare no competing financial interests.

Additional information

Supplementary information is available for this paper at https://doi.org/10.1038/s41593-017-0053-5.

Reprints and permissions information is available at www.nature.com/reprints.

Correspondence and requests for materials should be addressed to D.A.K.

Publisher's note: Springer Nature remains neutral with regard to jurisdictional claims in published maps and institutional affiliations

Methods

ENU screen. C57BL/6 male mice (*Mus musculus*) were given ENU injections and subsequently crossed with C3H/HeH females to generate G1 founder males. These founders were then out-crossed to C3H/HeH and the G2 daughters backcrossed to the G1 Founder male. Adult G3 mice aged approximately 16 weeks were killed for analysis and their brains postfixed in 4% paraformaldehyde (PFA) before dehydration in 30% sucrose. Brains were sectioned coronally (40 μm) and stereotaxically matched sections through the telencephalon (bregma –2.06 mm) were mounted on electrostatically charged slides and Nissl stained (0.6% cresyl violet). Sections were scanned using an Epson Perfection V750 Pro scanner and the following measurements recorded using the Image J software package: volume of the third ventricle and lateral ventricles; total brain volume; corpus callosum volume; thickness of the cortex; length of the pyramidal cell layer of the hippocampus; thickness of the molecular layer of the hippocampus; thickness of the stratum oriens of the hippocampus. For each genotype, at least 12 animals were analyzed.

Genetic mapping, exome sequencing and genotyping. DNA was extracted by standard techniques and 51 microsatellite markers covering all autosomes were amplified by PCR and visualized on agarose gels stained with ethidium bromide (4%). This established linkage to chromosome 9 between D9MIT11 and D9MIT81. Whole-exome sequencing was then performed using the Agilent whole-exome capture kit (SureSelectXT Mouse Kit, S0276129). Captured material was indexed and sequenced on the Illumina platform at the Wellcome Trust Sanger Institute. Exome sequence data were mapped to the mouse genome using Burrows–Wheeler Aligner (BWA) v0.5.9 and variants called using mPileUp within the SAMTools v0.1.19 suite[38]. The data has been submitted to the ENA (accession: ERS017958). The variant in Vps15 was confirmed by Sanger sequencing using the following primers: forward, AGTCCAACTGGCCTTAAACT; reverse, GTATAACCAAAATCCGCTCA, which were then employed to genotype animals for the subsequent studies. *Mbe/Mbe* animals were maintained on a C3H/He background. *Vps15*–conditional knockout animals were maintained on a C57/BL6 background. The Vps15 rescue line was created by injection of a modified BAC (RP24-281C16) into the pronuclei of B6CBAF1 zygotes. Transgenic founders were identified by PCR analysis (Supplementary Table 2) before crossing into the *Mbe* line. Animals were housed at the IMP/IMBA preclinical phenotyping facility with a maximum of six individuals per cage, with a 14-h light (6:00 to 20:00) and 10-h dark cycle.

Cellular studies. Mouse embryonic fibroblasts (MEFs) were prepared from E13.5 embryos. The body (without head or liver) was minced and incubated in 0.05% trypsin-EDTA at 37 °C for 10 min and then triturated with a pipette tip. The suspension was centrifuged at 800 rpm for 5 min and the cell pellet suspended in culture medium (DMEM supplemented with 10% FBS (FBS), 2% L-glutamine (Sigma, G7513), 1% PenStrep (Sigma, P0781) and 1% nonessential amino acids (Sigma, M7145). The following day, cells were trypsinized in 0.15% trypsin EDTA, passed through a 70-μm cell strainer and plated on gelatin-coated dishes. Human dermal fibroblasts were cultured in DMEM supplemented with 20% FBS, 1% L-glutamine, 1% PenStrep. For the EGFR degradation assay, cells were serum-starved in serum-free culture medium for 2 h. Culture medium was replaced with prewarmed uptake medium (DMEM supplemented with 2% L-glutamine, 1% PenStrep, 1% nonessential amino acids, 20 mM HEPES, 2% BSA and 100 ng/mL mouse EGF-488 (Thermo Fisher Scientific, E-13345)), and cells were incubated for the indicated time periods. Cells were washed twice with ice-cold 1× PBS, then lysed in ice-cold lysis buffer. Autophagy flux was assessed as previously described[39]. Cells were treated with 200 nM (MEFs) or 400 nM (HDFs) of the lysosomal inhibitor Bafilomycin A1. Autophagy flux was calculated by assessing the accumulation of LC3-II, 2 h and 4 h following lysosomal inhibition. Specifically, flux was calculated by: (LC3-II 2 h/Gapdh)/(LC3-II 0 h/Gapdh) and (LC3-II 4 h/Gapdh)/(LC3-II 2 h/Gapdh); $n = 3$ animals. The PDGF receptor degradation assay was performed as previously reported[16] ($n = 3$ animals per genotype, one or two technical replicates/timepoint). Mouse embryonic fibroblasts (MEFs) were starved in medium containing 0.2% BSA for 24 h, then treated with 20 μg/mL cycloheximide for 30 min before stimulation of receptor endocytosis by addition of 20 ng/mL PDGF-BB (Gibco, PMG0044) in starving medium supplemented with cycloheximide. At indicated timepoints, cells were washed twice with ice-cold 1× PBS and fixed in 4% PFA for 15 min, followed by permeabilization in 0.1% Triton X-100 in PBS. Cells were then incubated with primary antibody against PDGF receptor β (1:250, Cell Signaling #3169) followed by IRDye 800-labeled secondary antibody (LI-COR) and CellTag 700 stain (LI-COR) for normalization. Signal was detected using an Odyssey scanner (LI-COR). Signal from wells that were not treated with primary antibody was subtracted from the signal from sample wells, and empty wells were used for background subtraction. The half-life of PDGFR was calculated by fitting data to a one-phase decay curve using GraphPad Prism.

Rescue experiment in human cells. Human VPS15 cDNA was cloned into the pRRL lentiviral backbone downstream of a SFFV promoter[40]. For virus production, the transfer vectors psPAX2 (Addgene) and PMD2.G (Addgene) were transfected into Lenti-X (Clonetech) packaging cells. Human dermal fibroblasts

were transduced with concentrated virus at an efficiency of >90% as determined by mCherry expression. Four days after infection, cell lysates were prepared for western blot analysis.

Western blotting. Protein lysates were prepared in ice-cold RIPA buffer (10 mM TrisHCl pH 7.5, 150 mM NaCl, 1 mM EGTA, 1% sodium deoxycholate, 1% Triton X-100, 0.1% SDS) supplemented with protease and phosphatase inhibitor (Pierce #88668). Cells were incubated in lysis buffer for 15 min on ice before centrifugation. Frozen tissue samples were homogenized using a tungsten carbide bead in a Qiagen Tissue Lyser (2× 1 min, 20 Hz), incubated on ice for 1 h, then centrifuged twice for 20 min each time. Protein concentration was measured using a Pierce BCA Protein Assay Kit (#23225). Protein lysates were run on NuPAGE protein gels, blotted onto nitrocellulose or polyvinylidene fluoride membranes, blocked and probed with primary antibodies in 5% skimmed milk/TBST or 5% BSA/TBS. Antibodies targeting phosphoproteins were incubated with 1 mM sodium orthovanadate in 0.5% BSA/TBS. The following primary antibodies were used: 1:2,000 Vps15 for mouse studies (Novus Biologicals NBP1-30463)[39], 1:1,000 VPS15 for human studies (Abcam ab124817, Abcam ab128903)[41], 1:500 Vps34 (Cell Signaling, #3811)[42,43], 1:1,000 Beclin1 (Cell Signaling #3738)[44], 1:500 p62 (Novus Biologicals, H00008878-M01)[45], 1:2,000 GAPDH (Millipore, MAB374)[26,46], 1:1,000 α-tubulin (Santa Cruz, sc-8017)[47], 1:10,000 α-tubulin (Sigma Aldrich, T6199)[48], 1:100 LC3 (Nanotools, 0260-100/LC3-2G6)[49], 1:600 EGFR (Cell Signaling #4267 S)[50], 1:200 Nischarin (Santa Cruz, sc-365364)[21], 1:500 PAK1 T423 (Cell Signaling, #2601 S)[51] and 1:500 *N*-terminal Vps15 antibody (Proteintech, 17894-1-AP). Western blots were quantified using ImageJ. Western blots were replicated at least once, yielding similar results.

qPCR. qPCR was performed as previously described[52]. This involved the dissection of brains from embryos (E10.5, E12.5, E14.5, E16.5 and E18.5) and postnatal mice (P0, P6 and adult). Samples were then frozen before mRNA extraction and cDNA synthesis (SuperScript III First-Strand Synthesis System, Invitrogen, 18080-051). We used SYBR green on a Bio-Rad Cycler together with intron spanning primers to amplify *Vps15*, *Vps34*, *Beclin1* and *Nischarin* along with three control genes (*Pgk1*, *Tfrc* and *Hprt*; Supplementary Table 2). Reactions were performed in triplicate and the Ct values ascertained. The geometric mean of the control genes was calculated, permitting determination of ΔCt and the relative mRNA level[53,54]. For qPCR on human dermal fibroblast samples, qPCR used intron spanning primers to amplify *VPS15*, *VPS34*, *BECLIN1* and three control genes (Supplementary Table 2).

Whole-brain proteomics. Quantitative tandem mass tags (TMT) proteomics was performed in accordance with previously described protocols[55]. First, flash-frozen hippocampi were homogenized in a buffer containing 8 M urea with 200 mM ammonium bicarbonate using a Qiagen tissue lyser at 20 Hz twice for 1 min each time. Samples were then treated with TCEB at 56 °C for 30 min and 7.5 μL 5 mg/mL iodoacetamide solution for 30 min before dilution with 20 mM ABC and digestion with LysC (enzyme-to-protein ratio of 1:40 for 3 h at 37 °C). After this predigestion, samples were diluted with 200 mM ABC to a final urea concentration of 2 M. The tryptic digest was done with an enzyme-to-protein ratio of 1:40 for 2 h at 37 °C. Following desalting with C18 cartridges (Sep-Pak Vac 1 cc (50 mg)), samples were labeled with TMT in accordance with the manufacturer's specifications. TMT labeling reagents were equilibrated to room temperature and 41 μL of anhydrous acetonitrile added before incubation with the samples for 1 h. Strong cation exchange chromatography (SCX) was performed using an Ultimate system (Thermo Fisher Scientific) at a flow rate of 25 μL/min and a custom-made PolySULFOETHYL A (poly LC) column (5 μm particles, 300 Å, 1 mm i.d. × 250 mm). A total of 300 μg of peptide was loaded on the column, and 130 fractions were collected and stored at –80 °C. SCX fractions were then analyzed further using an UltiMate 3000 HPLC RSLCnano system (Thermo Fisher Scientific) coupled to a Q Exactive Plus mass spectrometer (Thermo Scientific) equipped with a Proxeon nanospray source. Fractions were loaded onto a trap column at a flow rate of 25 μL/min using 0.1% TFA as a mobile phase. After 10 min, the trap column was switched in line with the analytical column. Peptides were eluted using a flow rate of 230 nL/min and a binary 180-min gradient. The two-step gradient started with the mobile phases: 95% A (water/formic acid, 99.9/0.1, v/v) and 5% B (water/acetonitrile/formic acid, 19.92/80/0.08, v/v/v) increased to 10% B over the next 5 min and to 35% B over the next 55 min, followed by a gradient over 5 min to 90% B, where it was kept for 5 min, then decreased over 2 min back to the gradient 95% A and 5% B for equilibration at 30 °C. The Q Exactive Plus mass spectrometer was operated in data-dependent mode, using a full scan (m/z range 350–1,650, resolution of 70,000, target value 3×10^6) followed by MS/MS scans (resolution of 35,000, target value 1×10^6, maximum injection time 120 ms) of the 10 most abundant ions. MS/MS spectra were acquired using normalized collision energy 35% and an isolation width of 1.2 m/z. For detection of TMT reporter ions, a fixed first mass of 115 m/z was set for the MS/MS scans. Precursor ions selected for fragmentation were put on a dynamic exclusion list for 30 s. Raw data were processed in Proteome Discoverer (version 1.4.1.14, Thermo Fisher Scientific, Bremen, Germany) using MS Amanda (version 1.4.14.5564, FH OÖ/IMP, Austria) as a database search engine against the UniProt mouse database (20150830, 16,719 sequences) concatenated with a database of 298 contaminants provided with Proteome Discoverer. All acquired

SCX fractions were searched simultaneously using a precursor mass tolerance of 7 ppm and 0.03 Da fragment ion tolerance. Methylthiocysteine and 6plex-TMT at the N-terminus and lysine were specified as fixed modifications, whereas oxidation of methionine was set as dynamic modification. The result was filtered to 0.5% FDR using a Percolator algorithm integrated in Proteome Discoverer, and a minimum peptide sequence length of 7 and a minimum Amanda Score of 120 were required. To quantify TMT reporter ions, we used the integration method provided by Proteome Discoverer with a mass window of 5 ppm. Protein grouping was performed, applying strict maximum parsimony. Statistical significance of protein regulation was determined using LIMMA.

Immunohistochemistry. Mice were killed for analysis at E14.5, P0 and P11. Brains were fixed in 4% PFA overnight, dehydrated in 30% sucrose, and 12-μm sections were prepared. Adult mice aged 8 weeks and 4 months were perfused with 0.9% NaCl and 4% PFA and their brains postfixed for 6 h in 4% PFA. Following dehydration in 30% sucrose, 40-μm sections were prepared on a sledge microtome. Primary antibodies were diluted in 0.1–0.3% Triton-X100/PBS supplemented with 2% donkey serum (Abcam, ab7475) overnight at 4 °C (for fluorescence) or in 0.1–0.3% Triton-X100/PBS supplemented with 2% dry milk powder (for permanent staining). The following concentrations were used: 1:1,000 GFP (Abcam, ab13970)[56], 1:400 caspase-3 (Cell Signaling, #9661)[57], 1:500 LC3 (Nanotools, 0260-100/LC3-2G6), 1:500 p62 (Novus Biologicals, H00008878-M01), 1:300 Sox2 (Santa Cruz, sc-17320)[58], 1:300 Tbr2 (Millipore, AB15894)[59], 1:100 DCX (Santa Cruz, sc-8066)[60], 1:500 pH3 (Millipore, 06-570)[61], 1:300 nestin (BD Biosciences, #611658)[62], 1:300 NeuN (Millipore, MAB377)[63], 1:250 calbindin (Millipore, MAB1778)[64], 1:100 Cux1 (Santa Cruz, sc-6327)[7], 1:50 Nischarin (Santa Cruz, sc-365364), 1:1,000 Er81 (Jessell lab)[7], 1:300 FoxP2 (Abcam, ab16046)[7], 1:400 Prox1 (Millipore, MAB5654)[65], 1:500 GFAP (Dako, Z0334)[66], 1:2,000 calretinin (Swant, 6B3)[67] and 1:500 parvalbumin (Millipore, MAB1572)[68]. Where necessary, antigen retrieval was performed by heating sections to 90 °C in antigen retrieval buffer (Vector, H-3301), cooled at room temperature (20–25 °C) for 20 min and washed in 1× PBS before incubation with primary antibody. For Nischarin immunohistochemistry, sections were blocked with the Mouse on Mouse (M.O.M.) basic kit (Vector, MKB-2202). For the quantification of cleaved caspase-3, the total number of positive cells was counted manually in a 340-μm (E14.5) or 850-μm (P0 and P11) stretch of the cortex ($n = 3$ animals, 3 images/animal). For quantification of LC3 and p62, the numbers of cells positive for puncta were counted manually using the DAPI channel as a reference in a 200-μm broad region of the cortex ($n = 3$ animals, 3 images/animal). All counting was conducted blind to genotype.

Nissl and Golgi–Cox staining. For Nissl staining sections were incubated in 1% cresyl violet solution for 3–4 min, then washed and dehydrated in increasing ethanol concentrations. The cortical thickness was measured in Nissl-stained sections using ImageJ software. For each animal, we took three measurements in the somatosensory cortex and the visual cortex ($n = 3$ animals per genotype). Ectopic Nissl+ cells in the oriens layer of the hippocampus were quantified using ImageJ software by manually counting the number of pyramidal cells in the oriens layer and the pyramidal cell layer in a box of 310-μm edge length. For Golgi staining, mice aged 4 months were perfused with 0.9% NaCl and their brains treated with the Rapid GolgiStain Kit according to the manufacturer's instructions (FD Neurotechnologies, Inc., PK401). Dendritic spines were quantified as described[69]. In short, images of pyramidal neurons of the CA1 region of the hippocampus were captured using a Axioplan bright-field microscope. Spines located on tertiary apical dendritic branches in a single focal plane located at least 120 μm from the soma were quantitated ($n = 4$–6 neurons per animal ($n = 3$ animals per genotype). Neuron morphology was analyzed as previously reported[70]. Golgi–Cox impregnated 120-μm adult mouse brain sections were imaged in 1-μm z-intervals using a Axioplan bright-field microscope, and CA1 pyramidal neurons were traced in 3D using ImageJ's Simple Neurite Tracer plugin ($n = 3$ animals per genotype, 3 neurons each). Sholl analysis was performed using ImageJ's Sholl analysis tool. Concentric circles were chosen in 20-μm increments, centered on the soma. All quantification of Nissl stains and assessment of spines was performed blind to genotype.

Birthdate labeling experiments. Pregnant mice at E12.5, E14.5 and E16.5 were injected intraperitoneally with BrdU at 100 μg/g body weight. Offspring were killed for analysis at P0 and P11 and their brains were sectioned. After quenching (3% H_2O_2, 0.1% sodium azide, 5 min), antigen retrieval and acid treatment (2 N HCl, 37 °C, 70 min), sections were incubated with a primary antibody against BrdU (1:300, ABD Serotec, OBT0030) in 2% milk in 0.3% Triton X-100/PBS overnight. After washing, sections were incubated with a conjugated secondary antibody (Vector Laboratories, MP-7404) followed by peroxidase substrate (Vector Laboratories, SK-4105). The P0 cortex was divided into ten bins of the same size and the number of BrdU+ puncta counted manually in blinded images ($n = 3$ animals, 4–6 images/animal). For quantification of P11 brains, four regions of the hippocampus, equally spaced from rostral to caudal, were chosen for analysis. In each section, BrdU+ puncta were counted in the oriens layer, the pyramidal cell layer, the granule cell layer of the dentate gyrus and the hilus of the dentate gyrus

and expressed as relative to the total number of BrdU+ puncta in the hippocampal area ($n = 3$ animals, 8–10 images/animal). For BrdU/NeuN immunohistochemistry, sections were subject to antigen retrieval, acid treatment (2 N HCl, 37 °C, 45 min) and incubated with primary antibodies against BrdU (1:300, ABD Serotec, OBT0030) and NeuN (1:300, Millipore, MAB377) in 0.3% Triton X-100/PBS supplemented with 2% donkey serum (Abcam, ab7475) overnight. Three regions of the hippocampus equally spaced from rostral to caudal were chosen for analysis. The number of BrdU+NeuN+ cells in a 850 μm × 850 μm window of the CA1 region was counted. The percentage of ectopic BrdU+NeuN+ neurons in the oriens layer relative to the total number of BrdU+NeuN+ neurons was then calculated. All cell counting was performed blind to genotype. All histological procedures were carried out according to legal requirements and covered by an approved license (MA58/006093/2011/14) from the city of Vienna, Austria.

In utero electroporation experiments. The full-length sequences of Nischarin and Pak1 were amplified by PCR from a mouse brain cDNA library and cloned into the pCAGEN vector (Addgene). ShmiRNAs were cloned using the BLOCK-iT Pol II miR RNAi Expression Vector Kit (Invitrogen, K4936-00) according to the manufacturer's instructions. The knockdown efficiencies of shmiRNA constructs were determined following transfection into Neuro2A cells, FACS and western blot analysis. The control shmiRNA consisted of a scrambled sequence. The uteri of time-mated (E14.5), anesthetized C57/BL6J females were exposed after incision in the skin and peritoneum. Constructs supplemented with Fast Green tracer dye (Sigma Aldrich, F7252-5G) were injected into the lateral ventricle of the developing embryo. pCAGEN, pCAG-Cre (Addgene), pCAG-Nischarin and pCAG-Pak1T422E were injected at 0.5 μg/μL, pCAG-GFP (Addgene) at 0.2 μ g/μL and shmiRNA constructs at 1.9 μg/μL. Five 50-ms pulses of 36 V (950-ms intervals) were delivered using platinum electrodes coupled to a ECM830 (BTX) electroporator. Uterine horns were placed back into the abdomen and the incision closed with surgical sutures. The pregnant mouse was killed 3 d later by cervical dislocation and embryos collected for analysis. Following sectioning and staining with antibodies against GFP, images were captured and cell counting performed blind to the condition. A total of 2–5 images per mouse were counted using ImageJ.

Behavioral phenotyping. The behavioral testing of the mice started at age 12 weeks, and all tests were carried out chronologically as listed below on separate days. The open field was an enclosed arena consisting of gray PVC, measuring 50 cm long and 30 cm wide with 18-cm tall walls. The mouse was placed in a corner of the open field box, facing the wall, and tracked for 5 min. Distance travelled in the center, distance along the periphery and center entries were recorded. The elevated plus maze (EPM) consisted of two 29-cm long, 6-cm wide opposing open arms and two opposing enclosed arms 27 cm long and 6 cm wide at a height of 30 cm above the ground. The mouse was placed in the junction of the arms facing one of the closed arms and tracked for 5 min. We used the Anymaze software program (Stoelting Europe) to track the animals and extract the distance traveled, time spent in open and closed arms, and the number of entries. For rotarod assessment, mice were placed on the beam of the rotarod (Ugo Basile, Italy) facing in the direction opposite to rotation for 1 min at 5 rpm. Rotation speed was accelerated to a maximum of 30 rpm over 4 min. The latency before falling was measured up to a maximum of 6 min on the rod. Three trials were carried out with 1-h intervals[71]. For rewarded alternation, the T-maze consisted of one start arm and two goal arms each measuring 30 cm long, 10 cm wide and 29 cm tall. A food reward (condensed milk) was placed in each goal arm. Mice were food-deprived to 85% of their free-feeding weight. Mice were placed in the start arm facing the wall, and a free sample run was permitted. Following consumption of the food reward mice were placed back in the start arm and the rate of alternation recorded[72]. All behavioral phenotyping was performed blind to genotype. All animals were sex-matched littermates ($n = 11$ males, $n = 9$ females). Animals and their corresponding littermates were excluded in instances where the software tracking failed. All behavioral experiments were performed between 1 pm and 4 pm, during the animal's dark cycle, and were carried out according to legal requirements and covered by an approved license (MA58/002639/2008/5) from the city of Vienna, Austria.

Human genetics. Exome sequencing was performed on all family members (proband, mother, father and three siblings). The family was a Caucasian family from the Czech Republic. For exome enrichment, the NimbleGen SeqCap EZ v3.0 system was used according to the manufacturer's instructions. Adaptor-ligated libraries were then sequenced on an Illumina HiSeq 2000 instrument with a paired-end run of 101 bp to reach median coverage of 105×–140×. Image analysis, base calling and quality scoring were processed using the manufacturer's software Real Time Analysis (RTA 1.13.48) and FASTQ sequence files generated by CASAVA. Sequence reads were trimmed to the first base with a quality >30 and mapped to Human Genome build hg19 (GRCh37) using GEM mapper[73]. SAMtools suite version 0.1.18 was used to call single nucleotide variants and short indels. Variants on regions with low mappability[74], with read depth <10 or with strand bias $P < 0.001$ were filtered out. The population frequency of the variants was assessed by comparison to several databases: the 1,000 Genomes Project (http://www.1000genomes.org/), NHLBI Exome Sequencing Project (ESP) release

ESP5400 (http://evs.gs.washington.edu/EVS/), the ExAC genome browser and in-house databases. Variant annotation and functional prediction was performed with Annovar version 2011 Dec20, dbNSFP version light 1.3 and snpEff version 2.0.5d[75]. Unreported and rare coding variants were selected and subsequently filtered for various inheritance models (de novo, autosomal recessive, compound heterozygous and X-linked). The population frequency cut off was 1%, 0.1%, 2% and 1% for autosomal recessive, de novo, compound heterozygous and X-linked inheritance models, respectively. The mutation in VPS15 was confirmed by Sanger sequencing. This investigation was approved by the First Faculty of Medicine of the Charles University, Prague, Czech Republic. Informed consent was obtained from the family.

Statistics. All statistical analysis was executed in GraphPad Prism software package (v7.0c). For analysis of histological, western blot, cellular and behavioral data we performed either one-way ANOVA, two-way ANOVA, or *t* tests with post hoc comparisons (for example, Tukey tests). For analysis of our EGFR degradation assay, birthdate labeling experiments and rotarod results, we performed repeated-measures ANOVA with post hoc corrections. Datasets were checked for normality by Shapiro–Wilk tests. Where datasets were nonparametric transformations, Mann–Whitney or Kruskal–Wallis tests were applied. The statistical test applied for each experiment and the results obtained are shown in Supplementary Table 1. No statistical methods were used to predetermine sample sizes for our histological, behavioral and cellular experiments, but our sample sizes are similar to those reported in previous publications[7,39,52,71]. Samples and animals were not subject to randomization, but were assigned to experimental groups based on their genotype. In addition see the Life Sciences Reporting Summary.

Accession numbers. European Nucleotide Archive: ERS017958.

Life Sciences Reporting Summary. Further information on experimental design is available in the Life Sciences Reporting Summary.

Data availability. The data that support the findings of this study are available from the corresponding author upon reasonable request, with the exception of the human genetic data, which is subject to patient confidentiality. Whole-exome sequencing data of the *Mbe/Mbe* mouse has been archived by the Wellcome Trust Sanger Institute with accession code ERP000467 (http://www.sanger.ac.uk/datasharing/).

References

38. Li, H. & Durbin, R. Fast and accurate short read alignment with Burrows-Wheeler transform. *Bioinformatics.* **25**, 1754–1760 (2009).
39. Bejarano, E. et al. Connexins modulate autophagosome biogenesis. *Nat. Cell Biol.* **16**, 401–414 (2014).
40. Dull, T. et al. A third-generation lentivirus vector with a conditional packaging system. *J. Virol.* **72**, 8463–8471 (1998).
41. Sun, T. et al. Acetylation of Beclin 1 inhibits autophagosome maturation and promotes tumour growth. *Nat. Commun.* **6**, 7215 (2015).
42. Feng, W. et al. Dissection of autophagy in human platelets. *Autophagy* **10**, 642–651 (2014).
43. Ma, Y. et al. Toll-like receptor (TLR) 2 and TLR4 differentially regulate doxorubicin induced cardiomyopathy in mice. *PLoS ONE* **7**, e40763 (2012).
44. Lee, H. et al. Pathological roles of the VEGF/SphK pathway in Niemann-Pick type C neurons. *Nat. Commun.* **5**, 5514 (2014).
45. Willy, J. A. et al. Function of inhibitor of Bruton's tyrosine kinase isoform α (IBTKα) in nonalcoholic steatohepatitis links autophagy and the unfolded protein response. *J. Biol. Chem.* **292**, 14050–14065 (2017).
46. Jana, N. R., Tanaka, M., Wang, Gh & Nukina, N. Polyglutamine length-dependent interaction of Hsp40 and Hsp70 family chaperones with truncated N-terminal huntingtin: their role in suppression of aggregation and cellular toxicity. *Hum. Mol. Genet.* **9**, 2009–2018 (2000).
47. Santoh, M. et al. Acetaminophen induces accumulation of functional rat CYP3A via polyubiquitination dysfunction. *Sci. Rep.* **6**, 21373 (2016).
48. Rinaldi, C. et al. Insulinlike growth factor (IGF)-1 administration ameliorates disease manifestations in a mouse model of spinal and bulbar muscular atrophy. *Mol. Med.* **18**, 1261–1268 (2012).
49. Walls, K. C. et al. Lysosome dysfunction triggers Atg7-dependent neural apoptosis. *J. Biol. Chem.* **285**, 10497–10507 (2010).
50. Bertrand, T. et al. Conformations of tissue plasminogen activator (tPA) orchestrate neuronal survival by a crosstalk between EGFR and NMDAR. *Cell Death Dis.* **6**, e1924 (2015).
51. Li, S., Leshchyns'ka, I., Chernyshova, Y., Schachner, M. & Sytnyk, V. The neural cell adhesion molecule (NCAM) associates with and signals through p21-activated kinase 1 (Pak1). *J. Neurosci.* **33**, 790–803 (2013).
52. Breuss, M. et al. Mutations in the β-tubulin gene *TUBB5* cause microcephaly with structural brain abnormalities. *Cell Rep.* **2**, 1554–1562 (2012).
53. Vandesompele, J. et al. Accurate normalization of real-time quantitative RT-PCR data by geometric averaging of multiple internal control genes. *Genome Biol.* **3**, H0034 (2002).
54. Boda, E., Pini, A., Hoxha, E., Parolisi, R. & Tempia, F. Selection of reference genes for quantitative real-time RT-PCR studies in mouse brain. *J. Mol. Neurosci.* **37**, 238–253 (2009).
55. Pichler, P. et al. Peptide labeling with isobaric tags yields higher identification rates using iTRAQ 4-plex compared to TMT 6-plex and iTRAQ 8-plex on LTQ Orbitrap. *Anal. Chem.* **82**, 6549–6558 (2010).
56. Kita, Y., Kawakami, K., Takahashi, Y. & Murakami, F. Development of cerebellar neurons and glias revealed by in utero electroporation: Golgi-like labeling of cerebellar neurons and glias. *PLoS ONE* **8**, e70091 (2013).
57. Chu, Y. Y. et al. Astrocytic CCAAT/enhancer binding protein delta regulates neuronal viability and spatial learning ability via miR-135a. *Mol. Neurobiol.* **53**, 4173–4188 (2016).
58. Navarro-Quiroga, I., Hernandez-Valdes, M., Lin, S. L. & Naegele, J. R. Postnatal cellular contributions of the hippocampus subventricular zone to the dentate gyrus, corpus callosum, fimbria, and cerebral cortex. *J. Comp. Neurol.* **497**, 833–845 (2006).
59. Vasistha, N. A. et al. Cortical and clonal contribution of Tbr2 expressing progenitors in the developing mouse brain. *Cereb. Cortex* **25**, 3290–3302 (2015).
60. Boekhoorn, K. et al. Doublecortin (DCX) and doublecortin-like (DCL) are differentially expressed in the early but not late stages of murine neocortical development. *J. Comp. Neurol.* **507**, 1639–1652 (2008).
61. Hendzel, M. J. et al. Mitosis-specific phosphorylation of histone H3 initiates primarily within pericentromeric heterochromatin during G2 and spreads in an ordered fashion coincident with mitotic chromosome condensation. *Chromosoma* **106**, 348–360 (1997).
62. Shah, B. et al. C3G/Rapgef1 is required in multipolar neurons for the transition to a bipolar morphology during cortical development. *PLoS ONE* **11**, e0154174 (2016).
63. Mullen, R. J., Buck, C. R. & Smith, A. M. NeuN, a neuronal specific nuclear protein in vertebrates. *Development* **116**, 201–211 (1992).
64. Nóbrega, C. et al. Silencing mutant ataxin-3 rescues motor deficits and neuropathology in Machado-Joseph disease transgenic mice. *PLoS ONE* **8**, e52396 (2013).
65. Keays, D. A. et al. The role of Tuba1a in adult hippocampal neurogenesis and the formation of the dentate gyrus. *Dev. Neurosci.* **32**, 268–277 (2010).
66. Castellano, B. et al. A double staining technique for simultaneous demonstration of astrocytes and microglia in brain sections and astroglial cell cultures. *J. Histochem. Cytochem.* **39**, 561–568 (1991).
67. Gonchar, Y., Wang, Q. & Burkhalter, A. Multiple distinct subtypes of GABAergic neurons in mouse visual cortex identified by triple immunostaining. *Front. Neuroanat.* **1**, 3 (2008).
68. Gandal, M. J. et al. GABAB-mediated rescue of altered excitatory-inhibitory balance, gamma synchrony and behavioral deficits following constitutive NMDAR-hypofunction. *Transl. Psychiatry* **2**, e142 (2012).
69. Pillai, A. G. et al. Dendritic morphology of hippocampal and amygdalar neurons in adolescent mice is resilient to genetic differences in stress reactivity. *PLoS ONE* **7**, e38971 (2012).
70. Bas-Orth, C., Tan, Y. W., Oliveira, A. M., Bengtson, C. P. & Bading, H. The calmodulin-binding transcription activator CAMTA1 is required for long-term memory formation in mice. *Learn. Mem.* **23**, 313–321 (2016).
71. Oliver, P. L., Keays, D. A. & Davies, K. E. Behavioural characterisation of the robotic mouse mutant. *Behav. Brain Res.* **181**, 239–247 (2007).
72. Deacon, R. M. & Rawlins, J. N. T-maze alternation in the rodent. *Nat. Protoc.* **1**, 7–12 (2006).
73. Marco-Sola, S., Sammeth, M., Guigó, R. & Ribeca, P. The GEM mapper: fast, accurate and versatile alignment by filtration. *Nat. Methods* **9**, 1185–1188 (2012).
74. Derrien, T. et al. Fast computation and applications of genome mappability. *PLoS ONE* **7**, e30377 (2012).
75. Cingolani, P. et al. A program for annotating and predicting the effects of single nucleotide polymorphisms, SnpEff: SNPs in the genome of *Drosophila melanogaster* strain w1118; iso-2; iso-3. *Fly* **6**, 80–92 (2012).

naturereserach

Corresponding author(s):   David Keays

☐ Initial submission   ☒ Revised version   ☐ Final submission

Life Sciences Reporting Summary

Nature Research wishes to improve the reproducibility of the work that we publish. This form is intended for publication with all accepted life science papers and provides structure for consistency and transparency in reporting. Every life science submission will use this form; some list items might not apply to an individual manuscript, but all fields must be completed for clarity.

For further information on the points included in this form, see Reporting Life Sciences Research. For further information on Nature Research policies, including our data availability policy, see Authors & Referees and the Editorial Policy Checklist.

▶ Experimental design

1. Sample size

Describe how sample size was determined.

No statistical methods were used to pre-determine sample sizes for our histological, behavioural and cellular experiments but our sample sizes are similar to those reported in previous publications (Keays, Tian et al. 2007, Oliver, Keays et al. 2007, Breuss, Heng et al. 2012, Bejarano, Yuste et al. 2014).

2. Data exclusions

Describe any data exclusions.

Our initial experiments on human dermal fibroblasts were excluded as the cells tested positive for mycoplasm infection. These cells were treated with a Mycoplasm Removal Reagent containing a 4-oxoquinoline-3-carboxylic acid derivative. Following antibiotic treatment we confirmed on multiple occasions that our treated cells are mycoplasm negative (using a PCR based method). For our behavioural experiments animals and their corresponding littermates were excluded in instances where the software tracking failed.

3. Replication

Describe whether the experimental findings were reliably reproduced.

This is indicated in the figure legends for each Figure. Specifically, we replicated the data presented in:
- Figure 1 (d-i), Nissl staining and Marble rescue three times with similar results.
- Figure 2a, Quantification of Vps15, Vps34 and Beclin 1 from Mbe/Mbe, Mbe/+, +/+ animals twice with similar results.
- Figure 3d, quantification of Nischarin protein levels in Mbe/Mbe and +/+ animals twice with similar results.
- Figure 3g, quantification of activated Pak1 levels in Mbe/Mbe and +/+ animals twice with similar results.
- Figure 4a-i, NeuN and Calbindin staining on the hippocampus of Mbe/Mbe, Mbe/+, +/+ animals three times with similar results.
- Figure 5a-l, NeuN, Er81, Foxp2, and Cux1 staining on the cortex of Mbe/Mbe, Mbe/+, +/+ animals twice with similar results.
- Figure 6a-f, Nissl staining of +/fl, +/fl EMX1-Cre, fl/fl EMX1-Cre Vps15 animals twice with similar results.
- Figure 7e-i, western blot analysis of VPS15, VPS34, BECLIN1, and P62 in patients, were performed twice with similar results.
- Figure 7j-n, western blot analysis of VPS15, VPS34, BECLIN1, and P62 twice with similar results.

4. Randomization

Describe how samples/organisms/participants were allocated into experimental groups.

Subjects were defined by the genotype - so randomization was not necessary.

5. Blinding

Describe whether the investigators were blinded to group allocation during data collection and/or analysis.

We employed strict blinding procedures. For all our behavioral experiments phenotyping was performed blind to genotype. For all histological analysis and cell counting imaged sections were blinded randomly, and then analysed before the condition/genotype was revealed. This is stated in the methods.

Note: all studies involving animals and/or human research participants must disclose whether blinding and randomization were used.

6. Statistical parameters

For all figures and tables that use statistical methods, confirm that the following items are present in relevant figure legends (or in the Methods section if additional space is needed).

n/a	Confirmed
☐	☒ The <u>exact sample size</u> (*n*) for each experimental group/condition, given as a discrete number and unit of measurement (animals, litters, cultures, etc.)
☐	☒ A description of how samples were collected, noting whether measurements were taken from distinct samples or whether the same sample was measured repeatedly
☐	☒ A statement indicating how many times each experiment was replicated
☐	☒ The statistical test(s) used and whether they are one- or two-sided (note: only common tests should be described solely by name; more complex techniques should be described in the Methods section)
☐	☒ A description of any assumptions or corrections, such as an adjustment for multiple comparisons
☐	☒ The test results (e.g. *P* values) given as exact values whenever possible and with confidence intervals noted
☐	☒ A clear description of statistics including <u>central tendency</u> (e.g. median, mean) and <u>variation</u> (e.g. standard deviation, interquartile range)
☐	☒ Clearly defined error bars

See the web collection on statistics for biologists for further resources and guidance.

▶ Software

Policy information about availability of computer code

7. Software

Describe the software used to analyze the data in this study.	We employed Graphpad PRISM (v7.0c) for our statistical analysis, and ImageJ (v1.51) for our image analysis . For the analysis of our mouse exome sequencing data we used Burrows-Wheeler Aligner (BWA) v0.5.9 and variants were called using mPileUp within the SAMTools v0.1.19 suite39. For analysis of our proteomic data we used Proteome Discoverer (version 1.4.1.14) and MS Amanda (version 1.4.14.5564). For our analysis of human data we employed SamTools (v0.1.18), Illumina Real Time Analysis software (RTA 1.13.48), snpEff (v2.0.5d), dbNSFP (v1.3), GEM Mapper and Annovar (2011).

For manuscripts utilizing custom algorithms or software that are central to the paper but not yet described in the published literature, software must be made available to editors and reviewers upon request. We strongly encourage code deposition in a community repository (e.g. GitHub). *Nature Methods* guidance for providing algorithms and software for publication provides further information on this topic.

▶ Materials and reagents

Policy information about availability of materials

8. Materials availability

Indicate whether there are restrictions on availability of unique materials or if these materials are only available for distribution by a for-profit company.	There are no restrictions on the availability of materials.

9. Antibodies

Describe the antibodies used and how they were validated for use in the system under study (i.e. assay and species).

For our histological studies the following antibodies were used 1:1000 GFP (ab13970) (Kita, Kawakami et al. 2013), 1:400 caspase3 (Cell Signaling, #9661) (Chu, Ko et al. 2016), 1:500 LC3 (Nanotools, 0260-100/LC3-2G6), 1:500 p62 (Novus Biologicals, H00008878-M01), 1:300 Sox2 (Santa Cruz, sc-17320) (Navarro-Quiroga, Hernandez-Valdes et al. 2006), 1:300 Tbr2 (Millipore, AB15894) (Vasistha, Garcia-Moreno et al. 2014), 1:100 DCX (Santa Cruz, sc-8066) (Boekhoorn, Sarabdjitsingh et al. 2008), 1:500 pH3 (Millipore, 06-570) (Hendzel, Wei et al. 1997), 1:300 nestin (BD Biosciences, #611658) (Shah, Lutter et al. 2016), 1:300 NeuN (Millipore, MAB377) (Mullen, Buck et al. 1992), 1:250 calbindin (Millipore, AB1778) (Nobrega, Nascimento-Ferreira et al. 2013), 1:100 Cux1 (Santa Cruz, sc-6327) (Keays, Tian et al. 2007), 1:50 Nischarin (Santa Cruz, sc-365364), 1:1000 Er81 (Jessell lab) (Keays, Tian et al. 2007), 1:300 FoxP2 (abcam, ab16046)(Keays, Tian et al. 2007), 1:400 Prox1 (Millipore, MAB5654) (Keays, Cleak et al. 2010), 1:500 GFAP (Dako, Z0334) (Castellano, Gonzalez et al. 1991), 1:2000 Calretinin (Swant, 6B3) (Gonchar, Wang et al. 2007), 1:500 Parvalbumin (Millipore, MAB1572) (Gandal, Sisti et al. 2012). For our western blot studies the following antibodies were used: 1:2000 Vps15 for mouse studies (Novus Biologicals NBP1-30463) (Bejarano, Yuste et al. 2014), 1:1000 Vps15 for human studies (abcam ab124817, abcam ab128903) (Sun, Li et al. 2015), 1:500 Vps34 (Cell Signaling, #3811) (Ma, Zhang et al. 2012, Feng, Chang et al. 2014), 1:1000 Beclin1 (Cell Signaling #3738) (Lee, Lee et al. 2014), 1:500 p62 (Novus Biologicals, H00008878-M01) (Willy, Young et al. 2017), 1:2000 GAPDH (Millipore, MAB374) (Jana, Tanaka et al. 2000, Akizu, Cantagrel et al. 2015), 1:1000 Ubiquitin (Santa Cruz, sc-8017) (Santoh, Sanoh et al. 2016), 1:10000 alpha-tubulin (Sigma Aldrich, T6199) (Rinaldi, Bott et al. 2012), 1:100 LC3 (Nanotools, 0260-100/LC3-2G6) (Walls, Ghosh et al. 2010), 1:600 EGFR (Cell Signaling #4267S) (Bertrand, Lesept et al. 2015), 1:200 Nischarin (Santa Cruz, sc-365364) (Alahari, Reddig et al. 2004), 1:500 PAK1 T423 (Cell Signaling, #2601S) (Li, Leshchyns'ka et al. 2013), 1:500 N-terminal Vps15 antibody (Proteintech, 17894-1-AP).

10. Eukaryotic cell lines

a. State the source of each eukaryotic cell line used.

Neuro2A cells were employed to assess the efficiency of shmiRNA constructs and for antibody validation (Vps15 N-term). These cells were obtained from an in house supply at the IMP.

b. Describe the method of cell line authentication used.

qPCR analysis of neuronal markers is consistent with a mouse cell line of neuronal origin.

c. Report whether the cell lines were tested for mycoplasma contamination.

Cells were tested for mycoplasm contamination by our in house molecular biology service that employs a PCR based assay. All data presented in this manuscript is from mycoplasm negative cells.

d. If any of the cell lines used are listed in the database of commonly misidentified cell lines maintained by ICLAC, provide a scientific rationale for their use.

None of the cells used are in the ICLAC database.

▶ Animals and human research participants

Policy information about studies involving animals; when reporting animal research, follow the ARRIVE guidelines

11. Description of research animals

Provide details on animals and/or animal-derived materials used in the study.

For our ENU screen male C57BL/6 male mice (Mus musculus) were given ENU injections and subsequently crossed with C3H/HeH females to generate G1 founder males. These founders were then out-crossed to C3H/HeH and the G2 daughters backcrossed to the G1 Founder male. Adult G3 mice aged approximately 16 weeks were sacrificed and subject to phenotypic analysis. Following the identification of the Marble line it was maintained on a C3H/HeH background. Vps15 KO animals were maintained on a C57/BL6J background. For our behavioral experiments we employed n=20 animals with sex matched littermate pairs (n=9 females, n=11 males). Behavioral testing was performed on animals aged 12 weeks. Histological analysis of the Marble and Vps15 KO lines was performed on animals aged E14.5, P0, P11, 8 weeks and 4 months (n=3-6). Our histological analysis employing the Golgi method was performed on animals aged 4 months (n=3 animals per genotype). For our cellular experiments mouse embryonic fibroblasts (MEFs) were prepared from E13.5 embryos of all three genotypes (+/+, +/Mbe, Mbe/Mbe) (n=3). For our qPCR studies we employed tissue isolated from C57/BL6J animals aged E10.5, E12.5, E14.5, E16.5, E18.5 and postnatal mice P0, P6 and 8 weeks (n=3). For our in utero electroporation studies we used pregnant C57/BL6J females. Embryos were electroporated at E14.5, and then analyzed a E17.5 (n=3-6). The Vps15 rescue line was created by injection of a BAC (RP24-281C16) into the pronuclei of B6CBAF1 zygotes.

Policy information about studies involving human research participants

12. Description of human research participants

Describe the covariate-relevant population characteristics of the human research participants.

We report all the relevant clinical details with respect to the patient with the L1224R mutation in Vps15 in the results of this manuscript. Specifically, the affected individual presented with severe cortical and optic nerve atrophy, localized cortical dysplasia, intellectual impairment, spasticity, ataxia, psychomotor delay, muscle wasting, pseudobulbar palsy, a mild hearing deficit and late onset epilepsy. He was homozygous for the L1224R mutation, whereas he parents were heterozygous.